The Influence of Dopants & Particles on the Kinetics of Microstructural Evolution of Alumina

Ruth Moshe

The Influence of Dopants & Particles on the Kinetics of Microstructural Evolution of Alumina

Research Thesis

In Partial Fulfillment of the

Requirements for the Degree of

Doctor of Philosophy

Ruth Moshe

Submitted to the Senate of the Technion-Israel Institute of Technology

Cheshvan 5780 Haifa November 2019

The research thesis was done under the supervision of **Prof. W.D Kaplan** in the Department of Materials Science & Engineering at the Technion.

Acknowledgements

I wish to thank the Technion for partial financial support of this study. This research was partially supported by the Israel Science Foundation (grant No. 1779/18). Also, I gratefully acknowledge the financial support of the Irwin and Joan Jacobs fellowship and the Rosa and Harry Shayn fellowship.

List of Publications:

1. R. Moshe, A. Berner, W. D. Kaplan, The Solubility Limit of SiO_2 in α-alumina at 1600°C, Scripta Materialia **86**, 40-43 (2014).
2. R. Moshe, W. D. Kaplan, The Influence of CaO on Alumina Grain Boundary Mobility, Journal of the European Ceramic Society **39**, 1324-1328 (2019).
3. R. Moshe, W. D. Kaplan, The Combined Influence of Mg and Ca on Microstructural Evolution of Alumina, Journal of the American Ceramic Society 102, 4882-4887 (2019).

Table of Contents

Abstract 1

List of Symbols and Abbreviations 3

1. Literature Survey 7

1.1 Grain Boundary Mobility and Microstructural Evolution 7

1.1.1 Grain Boundary Mobility Measurements 9

1.2 Segregation and Complexions 10

1.3 Solute Drag and Zener Drag 12

1.3.1 Solute Drag 13

1.3.2 Second Phase Particles 14

1.4 Disconnections as the Mechanism for Grain Boundary Motion 16

1.5 Alumina 17

1.5.1 Solid State Sintering 19

1.5.2 Grain Growth of Alumina 19

2. Research Goals 24

3. Experimental Methods 25

3.1 Alumina Processing 26

3.1.1 Solubility Limits of Dopants in Alumina at 1600°C 27

3.1.2 Grain Boundary Mobility in Ca Doped Alumina 29

Table of Contents (Continued)

3.1.3 Grain Boundary Mobility in Ni-Alumina Composites 30

3.1.4 The Influence of Dopants on Ni Occlusion in Ni-Alumina Composites 31

3.2 Characterization 31

3.2.1 X-Ray Diffraction and Energy Dispersive Spectroscopy 31

3.2.2 TEM and HRS/TEM-EDS 32

3.2.3 WDS 32

4. Results 34

4.1 Solubility Limits of Dopants in Alumina at 1600°C 34

4.1.1 SiO_2 in Alumina 34

4.1.2 Alumina Co-Doped with MgO and CaO 36

4.2 Grain Boundary Mobility in Ca Doped Alumina 41

4.2.1 Chemical Characterization 41

4.2.2 Mobility Measurements 45

4.3 Grain Boundary Mobility in Ni-Alumina Composites 47

4.3.1 Chemical Characterization 47

4.3.2 Mobility Measurements 48

4.4 The Influence of Dopants on Ni Occlusion in Ni-Alumina Composites 51

5. Discussion 55

Table of Contents (Continued)

5.1 The Influence of Solute on Mobility 55

5.2 The Influence of Solute on Alumina 57

5.2.1 Solute Drag 57

5.2.2 Solute Acceleration 58

5.3 Influence of Solute Concentration Near the Solubility Limit on Mobility 62

5.4 The Influence of Solute on Alumina Composites 64

5.4.1 Solute Acceleration and Zener Drag 64

5.4.2 The Influence of a Solute on Occlusion 69

6. Summary and Conclusions 71

7. Recommendations for Future Work 73

8. References 75

List of Figures

Figure 1: Schematic drawing of grain boundary movement by atom migration from one orientation to the other, as a result of a pressure difference caused by (a) curvature and (b) WMC. 8

Figure 2: Schematic drawings of possible interactions between a second phase particle (or pore) and a grain boundary. (a) When the grain boundary migration rate exceeds the particle mobility ($M_{GB}>M_p$) a process of separation of the particle from the moving grain boundary occurs, and the particle eventually becomes occluded by the growing grain. (b) When $M_{GB}=M_p$ the grain boundary mobility is limited by the particle mobility. 16

Figure 3: XRD pattern confirming the presence of only mullite ($3Al_2O_3 \cdot 2SiO_2$) and alumina, thus ensuring saturation of the alumina grains with Si. 34

Figure 4: BSE SEM micrograph of an alumina sample doped with SiO_2, which underwent liquid phase sintering until the SiO_2 reacted with alumina to form crystalline mullite. 35

Figure 5: Histogram of the Si concentration measurements from the specimens quenched from 1600°C. 36

Figure 6: XRD pattern confirming the presence of alumina, and binary and ternary phases, thus ensuring saturation of the alumina grains with Mg and Ca. 37

List of Figures (Continued)

Figure 7: BSE SEM micrograph of an alumina sample doped with CaO and MgO, which underwent sintering until the CaO and MgO reacted with alumina to form crystalline CAM-II. 38

Figure 8: Bright field TEM micrograph of a CAM-II precipitate. 38

Figure 9: Histogram of the Ca concentration measurements from the specimens quenched from 1600°C. 40

Figure 10: Histogram of the Mg concentration measurements from the specimens quenched from 1600°C. 40

Figure 11: XRD pattern of alumina doped with 47 ppm of CaO, showing only reflections from α-Al_2O_3, i.e. no reflections from $CaO_6Al_2O_3$ (CA6) are detectable. 41

Figure 12: Histograms of Ca concentration measurements from undoped and doped specimens sintered at 1600°C for 2 h in He: (a) trace (3±1 ppm) of Ca in the undoped sample; (b) 9±1 ppm of Ca in doped alumina; (c) 15±2 ppm of Ca in doped alumina; (d) 47±1 ppm of Ca in a doped alumina. 42

Figure 13: HRSTEM micrograph of a GB in alumina doped with 47±1 ppm of Ca. 44

Figure 14: (a) HAADF-STEM micrograph of alumina GB in alumina sample doped with 47 ppm of Ca. (b)-(d) EDS elemental map of Al, O and Ca acquired simultaneously with the micrograph presented in (a). 45

Figure 15: BSE SEM micrograph of the microstructure of alumina doped with 47ppm Ca and annealed at 1600°C for 10 hours. 46

List of Figures (Continued)

Figure 16: Effective grain boundary mobility of undoped alumina and alumina doped with 9, 15 and 47 ppm of Ca, annealed at 1600°C in He (marked ■), compared with the effective grain boundary mobility of undoped alumina and alumina doped with 13 ppm of Ca determined by Akiva et al. (marked ●) [11]. 47

Figure 17: Backscattered HRSEM micrograph of the microstructure of Ni-alumina. 49

Figure 18: Grain size as function of time of undoped alumina and alumina doped with 15 ppm of Ca, compared with the grain size as function of time of undoped Ni-alumina and Ni-alumina doped with 18 ppm of Ca. 49

Figure 19: The effective grain boundary mobility as a function of dopant concentration (calcium) of alumina (marked ▼), and Ni-alumina (marked ■). 50

Figure 20: STEM EDS tomography micrograph of Ni particles at alumina GB. The curved facets indicate that the particles were dragged by alumina GBs. 50

Figure 21: Grain size as function of time for undoped Ni alumina composites compared with the grain size as function of time of Ni alumina composites doped with 18 ppm of Ca. 51

Figure 22: SE HRSEM micrograph of the microstructure of Ni-alumina doped with Cr_2O_3 and MgO. 52

Figure 23: SE HRSEM micrograph of the fracture surface of Ni-alumina doped with Cr_2O_3 and MgO. 52

List of Figures (Continued)

Figure 24: BF TEM micrograph of Ni-alumina doped with Cr_2O_3 and MgO. 53

Figure 25: Ni particle size in Al_2O_3 doped with MgO and Cr_2O_3. 53

Figure 26: The influence of composition on the mobility of a single grain boundary. 56

Figure 27: The influence of composition on the mobility in a polycrystalline material (with many grain boundaries). 56

Figure 28: A schematic representation of the influence of Mg and/or Ca on grain growth of alumina as single species and in co-doping conditions. 69

List of Tables

Table 1: EDS measurement from a mullite grain detected in the quenched sample (see arrow in Figure 5), confirming the XRD results that a two phase system formed. 35

Table 2: EDS measurement from a CAM-II grain detected in the quenched sample (as shown in Figure 9), confirming the XRD results that the ternary $Ca_2Mg_2Al_{28}O_{46}$ phase formed. 39

Table 3: WDS measurements from alumina doped with various amounts of Ca, which was used to determine the actual Ca concentration of each sample. 43

Table 4: Ca concentration determined by WDS measurements and Ca GB excess measurements. 45

Table 5: Ni particle size and percent of occluded particles for Mg doped alumina, with Cr ..54

Table 6: The influence of Mg and Ca on grain growth of alumina as single species and in co-doping conditions. 68

Abstract

The solute drag theory predicts that the presence of solutes in a material will hinder grain boundary movement. However, there are several systems that when doping with specific solutes, the grain boundary mobility increases. In this study, the influence of CaO on the evolving microstructure of alumina and Ni-alumina composites has been studied in a range of concentrations below the solubility limit. The amount of Ca in the alumina was determined by conducting fully standardized wavelength dispersive spectroscopy, and the change in grain boundary mobility as a function of the amount of dopant was characterized using scanning electron microscopy. Unlike segregating dopants which reduce grain boundary mobility by solute-drag, CaO increases the rate of grain growth, and a trend of increased mobility with increasing dopant level was shown. The increased mobility with Ca segregation is believed to be due to an increase in vacancy concentration in the vicinity of the grain boundaries, thus facilitating faster grain boundary motion.

In addition, the solubility limits of Ca and Mg in co-doped alumina and of Si in alumina were measured using wavelength dispersive spectroscopy on a scanning electron microscope. For the determination of the solubility limit of Si in alumina at 1600°C, samples were doped with Si such that the equilibrated material would contain two phases: $3Al_2O_3 \cdot 2SiO_2$ (mullite) and alumina saturated with Si. Thus, the amount of Si measured in the alumina grains represents the solubility limit. Measurements were conducted on water-quenched and furnace-cooled samples. For the quenched samples the Si solubility limit in Al_2O_3 was found to be 188±7 ppm at 1600°C.

In a similar manner the solubility limits of Ca and Mg co-doped in alumina at 1600°C were determined by equilibrating alumina saturated with Ca and Mg. This resulted in the formation of $MgAl_2O_4$ (Mg spinel), $CaO{\cdot}6Al_2O_3$ (CA6), $Ca_2Mg_2Al_{28}O_{46}$ (CAM-II) and alumina grains saturated with Mg and Ca. Under these conditions, the amount of Ca and Mg in the alumina grains represents the solubility limits. In the co-doped state, the solubility limit of Ca in alumina was 32±13 ppm, and the solubility limit of Mg in alumina was 210±43 ppm. The presence of Ca results in an increase of the solubility limit of Mg in alumina from 132 ppm to 210 ppm, suggesting that the increased Mg in solution results in more Mg excess at the alumina grain boundaries, thus contributing to a decreased grain boundary mobility by solute-drag.

List of Symbols and Abbreviations

A	Interface area
A_{Al}, A_{Ca},	Atomic masses of Al and Ca
AGG	Abnormal grain growth
at.%	Atomic percent
BSE	Backscattered electron
C_{∞}	Bulk solute concentration
C_0	Solute concentration in the bulk
CA6	Ca Hexaaluminate ($cao \cdot 6Al_2O_3$)
CAM-II	$Ca_2Mg_2Al_{28}O_{46}$
CIP	Cold isostatic pressing
$C_{lim,0.975}$	Limit of detection with a confidence probability of 97.5%.
C_{std}	Concentration in a standard sample
D_{GB}	Diffusion coefficient for atomic motion across the grain boundary of matrix atoms
D_S	Diffusion coefficient for solute atoms
$D_{surface}$	Surface diffusivity
EDS	Energy dispersive spectroscopy
$f[\Gamma]$	Grain boundary segregation factor

F_0	Intrinsic drag force
F_{GB}	Curvature-induced driving force
F_s	Solute drag force
F_Z	Zener drag force
G	Grain size
GB	Grain boundary
G_v	Gibbs volume energy
$H^{formation}$	Enthalpy of formation
HPA	High purity alumina
HRSTEM	High resolution scanning transmission electron microscopy
I	Intensity
IGF	Intergranular film
k	Boltzmann constant
$k_{Ca/Al}$	K-factor for element Ca in alumina
m	Number of measurements
M_{GB}	Grain boundary mobility
M_i	Intrinsic grain boundary mobility
M_p	Particle or pore mobility
M_S	Grain boundary mobility due to solute drag

N_z	Particle or pore density at the grain boundary
P	Pressure
Pa	Pascal
pH	Power of hydrogen
ppm	Parts per million
r	Particle or pore radius
r_1 ,r_2	Radii of curvature perpendicular with each other at the interface between adjacent grains
r^{crit}	Critical radius for homogenous nucleation
SE	Secondary electron
SEM	Scanning electron microscopy
STEM	Scanning transmission electron microscopy
T	Temperature
t	Time
TEM	Transmission electron microscopy
T_m	Melting temperature
V/S	Ratio between the interaction volume and the area of the GB inside the interaction volume
V_{GB}	Grain boundary velocity
WDS	Wavelength dispersive spectroscopy
WMC	Weighted mean curvature

wt.%	Weight percent
XRD	X-ray diffraction
YAG	Yttrium aluminum garnet
α-Al_2O_3	Alumina structure
α_s	Solute drag per unit velocity and per unit dopant concentration
α	Geometrical factor that depends on the shape of the boundary
β	Drift velocity
$\delta_{surface}$	Surface thickness
δ_{GB}	Grain boundary width
Γ_{min}	Limit of detection
Γ	Surface or interface excess concentration
γ_{GB}	Grain boundary energy
γ	Surface or interface energy
μ	Chemical potential
θ	Dihedral angle
ρ	Density
τ	Measurement time
Ω	Atomic volume

1. Literature Survey

1.1 Grain Boundary Mobility and Microstructural Evolution

Grain growth takes place when a grain boundary (GB) migrates in order to decrease the total grain boundary area and thus the total free energy of the system. A process of short-range diffusion, where atoms or ions move across the boundary and join the orientation of the growing grain, brings about the movement of the grain boundary. Consequently, the direction of flux is opposite to that of grain boundary motion (Figure 1(a)). The difference in chemical potential is the local driving force for grain boundary movement. It correlates with boundary curvature which presents a pressure difference between adjacent grains [1]:

$$\Delta P = \gamma_{GB}\left(\frac{1}{r_1} + \frac{1}{r_2}\right) = \frac{\alpha\gamma_{GB}}{G} \qquad \textbf{(1)}$$

where ΔP is the difference in pressure between adjacent grains, γ_{GB} is the grain boundary energy, r_1 and r_2 are the principal radii of curvature perpendicular with each other at the interface between the adjacent grains, α is a geometrical factor that depends on the shape of the boundary, and G is the grain size. To deal with faceted boundaries (and surfaces), the weighted mean curvature (WMC) is a theory that suggests calculating the average curvature of faceted planes while considering the surface energy of the faceted planes [2]. The difference in pressure from equation (1) is thus translated as the rate of decrease of surface energy with respect to the volume swept out by the motion of the faceted shape, showing that the driving force for migration is a change in the free energy per unit area.

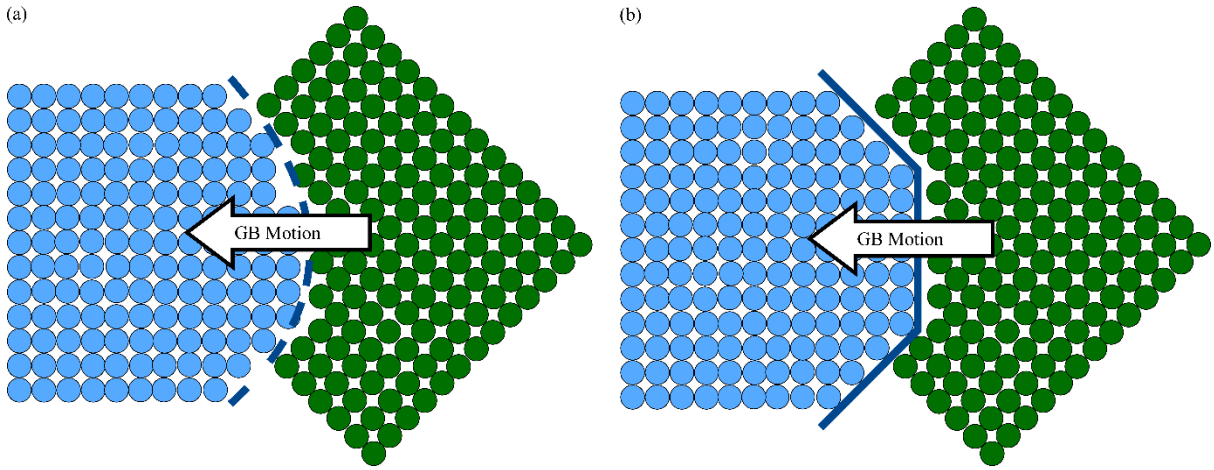

Figure 1: Schematic drawing of grain boundary movement by atom migration from one orientation to the other, as a result of a pressure difference caused by (a) curvature and (b) WMC.

Grain boundary migration, in a single phase system, will transpire due to the WMC-induced driving force (F_{GB}) at a velocity of V_{GB}. This driving force will balance out at steady state with a drag force. Drag forces may be introduced depending on different interactions between the microstructure and the grain boundary in the form of intrinsic drag, solute drag and/or pore/precipitate drag (ignoring external fields). Since V_{GB} and F_{GB} depend on each other, and may vary widely in the same system, normalization is commonly used and the grain boundary mobility is defined as [3]:

$$M_{GB} = \frac{V_{GB}}{F_{GB}} \qquad \textbf{(2)}$$

Applying this enables one to distinguish between cases in which a change in the driving force only produces a velocity difference (M_{GB} remains constant), and cases in which the mechanism for grain growth has changed and a difference in grain boundary mobility is evident. Various

causes for migration mechanism changes will be discussed in the scope of this work. At the outset, the intrinsic grain boundary mobility will be presented.

The intrinsic grain boundary mobility depends on the rate of transport of atoms or ions of the grain across the boundary. This results in an intrinsic drag force F_0 without any other sources of drag, thus rendering F_0 equivalent to atom diffusion under the chemical potential gradient (μ) that resides across the grain boundary width (δ_{GB}) [3]:

$$F_0 = \frac{d\mu}{dx} = \frac{d(\Omega\Delta P)}{dx} = \frac{1}{\delta_{GB}}\frac{\Omega\gamma_{GB}\alpha}{G} \quad \textbf{(3)}$$

where Ω is the atomic volume.

According to Burke and Turnbull's model, grain boundary velocity is approximately equal to the instantaneous grain growth rate [4]. Incorporating this assumption with the intrinsic drag force, taken as a pressure difference, and a chemical potential gradient across the grain boundary, results in the intrinsic mobility [5]:

$$M_i = \frac{D_{GB}}{kT}\left(\frac{\Omega}{\delta_{GB}}\right) \quad \textbf{(4)}$$

where D_{GB} is the diffusion coefficient for atomic motion across the grain boundary, k is the Boltzmann constant and T is the temperature.

1.1.1 Grain Boundary Mobility Measurements

The measurement of grain boundary mobility of ceramics introduces difficulties, since 100% pure ceramics do not exist. The powder used for sintering a ceramic material will always

contain some level of impurities. The presence of impurities can have a significant effect on the mobility of the grain boundaries. However, many studies have reported a measurement of grain boundary mobility in undoped samples despite this limitation, and have not dealt directly with the influence of trace elements in the starting powder.

Mobility measurements are often carried out by measuring the change in average grain size, after a series of annealing treatments that induce grain growth are performed on the sample. This allows for an expression of the velocity of the grain boundary [3]:

$$V_{GB} = \frac{d\overline{G}}{dt} = \frac{2M_{GB}\gamma_{GB}}{\overline{G}} \quad \textbf{(5)}$$

Assuming spherical grains and equiaxed growth, α=2. Integration of equation (5) produces the grain growth law [3]:

$$\overline{G}_t^2 - \overline{G}_0^2 = 4M_{GB}\gamma_{GB}t = kt \quad \textbf{(6)}$$

where $\overline{G}_t^2$ is the average squared grain size at time t, $\overline{G}_0^2$ is the average squared grain size at t=0 and k is the rate constant. Derived from the grain growth law, the term for effective mobility is defined as $M_{GB}\gamma_{GB} = \frac{k}{4}$. Using the above technique, one can determine in a relatively fast manner the mean effective mobility.

1.2 Segregation and Complexions

Grain boundary mobility can be affected by the chemistry and/or structure of the GB (and the chemical potential gradient across the grain boundary). A dopant or impurity in solution at a concentration below the solubility limit (referred to as a solute) in a polycrystalline material will undergo equilibrium segregation to grain boundaries (or any planar defect) if the presence

of the solute at the planar defect reduces its surface energy. Solute segregation therefore changes the chemical composition of the grain boundary and may influence GB/interface energy. Gibbs correlated adsorption and surface energy and suggested the following isotherm [6]:

$$d\gamma = -\sum_{i} \Gamma_i \, d\mu_i \qquad \textbf{(7)}$$

where Γ_i is the specific surface excess of component i and μ_i is the chemical potential of component i. In his description, Gibbs demonstrated that adsorption will occur if it reduces energy. At the same time, equation (7) lacks a direct correlation to the bulk solute concentration (unless the solution is assumed to be dilute or ideal). To this end more explicit isotherms were developed. Following Gibbs, Bishop et al. hypothesized the diffuse interface theory where they discussed the concentration at the surface and hypothetically correlated it to the activity [6]. They showed that an increase in solute excess at the interface is expected as the bulk solute concentration increases up to the solubility limit. Above the solubility limit is the two phase region, and precipitation occurs [6]. Expanding on Gibbs, Seah and Hondros further described GB segregation. They hypothesized that the grain boundary excess is linked to the solute bulk concentration as is the energy it would take for precipitation to occur at the solubility limit [7]. In doing so, they suggested a correlation between an increase of solute bulk concentration, to an increase in solute atoms undergoing segregation to GBs.

Pursuant to understanding segregation and its influence on GB characteristics, the term "complexion" was coined. Complexions describe an equilibrium 2D state of an interface (including grain boundaries, free surfaces, or planar defects) with a specific atomistic structure *and* chemistry associated with the dopant activity in the bulk. As in Gibbsian segregation,

these 2D structures display transitions which have been shown to significantly influence the grain boundary properties, specifically the mobility of the grain boundary during grain growth [8]. While analogous to bulk phases, complexions can only exist at a bulk phase surface or at an interface between two bulk phases. Also, complexion transitions do not depend on bulk transitions in adjacent bulk phases. At grain boundaries, a first order complexion transition may be identified by locating a highly localized (2D) structural change or by measuring an abrupt change in the adsorption content as a function of solute concentration. The complexion's width is determined by thermodynamic equilibrium. However, while the width is a characteristic of the complexion it does not classify it, in the same manner that classical Gibbsian segregation transitions are not classified by the thickness of segregated atomic layers [9]. The presence of specific complexions may be accompanied by a change in properties such as grain boundary mobility, electrical conductivity and adhesion [9]. In summary, complexions are a convenient approach to describing both the chemical and structural excess of surfaces, and are similar to the classical Gibbsian approach to adsorption.

1.3 Solute Drag and Zener Drag

Intrinsic mobility does not take into account the influence of dopants, impurities, second phase particles and porosity. Theoretical calculations and experimental studies have shown that grain boundary mobility is strongly affected by these microstructural variants; actual grain boundary mobility had been assumed to be a third of that calculated for intrinsic mobility [10]. However, recent measurements have presented conflicting reports and deduced that grain boundary mobility can be *enhanced* due to solute segregation [11]. Prior to considering the influence of

the microstructural variants on the evolving microstructure, an examination of their influence on the grain boundary mobility is given.

1.3.1 Solute Drag

Segregation of solute atoms to a grain boundary and/or interface will occur in a situation where it will reduce the surface excess energy, and thus the total energy of the system. Movement of a grain boundary with an equilibrated segregation profile can create a concentration profile at the plane of the boundary which deviates from the equilibrium state, due to the attracting and repulsive forces between the solute atoms and the atoms at the grain boundary. It was presumed that this asymmetry introduces a drag force on the grain boundary which reduces the migration rate. A boundary may eventually break away from a high concentration of solute, if the driving force for migration is high enough. At this point, according to the solute drag theory, the grain boundary mobility will return to its intrinsic value. The solute drag force has been described by several models [10,12,,14], where Cahn calculated the solute drag force (F_s) as a function of distance from the grain boundary:

$$F_s = \frac{\alpha_s C_\infty v_{GB}}{1 + \beta^2 {v_{GB}}^2} \qquad \textbf{(8)}$$

where α_s is the solute drag per unit velocity and per unit dopant concentration in the low boundary velocity limit, β^{-1} is the drift velocity with which an impurity diffuses across the grain boundary, and C_∞ is the bulk solute concentration. α will be of a similar value whether an attractive or repulsive interaction energy of the same magnitude exists between the solute and the grain boundary. In steady state, the total drag force is thus assumed to be the sum of intrinsic drag (F_0) and the solute drag force (F_s). As mentioned above, the mobility due to solute drag is initially constant; if the boundary detaches from the solute cloud then the migration rate returns

to intrinsic values. Previous direct observations indicated that the increase in grain boundary mobility is not uniform, but rather has a start-and-stop motion which was assumed to reflect transitions between the solute drag and intrinsic mobility values [15,16]. In the region where solute drag is most prominent the mobility due to solute drag is defined:

$$M_S = \left(\frac{\Omega}{kT\delta_{GB}}\right)\left(\frac{1}{D_{GB}} + \frac{4C_0 f(\Gamma)}{D_S}\right)^{-1} \quad \textbf{(9)}$$

where D_S is the diffusion coefficient for solute atoms, C_0 is the solute concentration in the bulk and $f(\Gamma)$ is the grain boundary segregation factor. The mechanism for atom movement assumed to facilitate this model is that of random 'jumping' of atoms from one grain to other. It is assumed that atoms randomly change their configuration from one grains' orientation to the other. Therefore, it is also assumed that when solute atoms segregate to the GB, they change the GB solute profile symmetry, and this slows down the rate of atomic 'jump'. Although this model explains how a decrease in mobility is expected when solute is introduced to the system, it is limited and does not presume to account for solute acceleration. Also, a broader understanding of the mechanism for GB movement has been realized since the solute drag theory was contemplated, stipulating revisiting the solute drag theory, as will be discussed in this work.

1.3.2 Second Phase Particles

The influence of a second phase on the grain boundary velocity was initially considered by Zener [17]. A drag force (F_Z) introduced by a particle with radius r interacting with a grain boundary with energy γ_{GB} induces a pinning force. This drag force may be expressed as:

$$F_Z = \pi r \gamma_{GB} \cdot (17.9 - 6.2\psi) \quad \textbf{(10)}$$

where ψ is the dihedral angle. In Zener's model a pinning effect is discussed, under the assumption that the second phase particle does not migrate with the boundary. However, a second phase particle velocity may be defined and a Zener-type analysis may be applied to migrating second phase particles. This analysis is similar in nature for examining the interaction between a grain boundary and a pore, or a grain boundary and a precipitate, although generally the velocity of a particle will be lower than that of a pore [3,5].

The grain boundary curvature applies a force on the pore which changes its shape and introduces a flux of matter. The flux results in movement of the pore in the direction of the boundary. The mobility of the pore is controlled by the rate of atoms transporting from the leading surface to the trailing surface:

$$M_p = \frac{D_{surface}\delta_{surface}\Omega}{kT\pi r^4} \quad \textbf{(11)}$$

where $D_{surface}$ is the surface diffusivity and $\delta_{surface}$ is the surface thickness. Considering a maximum drag force F_z, given in equation (10), the grain boundary velocity is calculated as:

$$V_{GB} = M_{GB}(F_{GB} - N_z F_z) \quad \textbf{(12)}$$

where N_z is the particle or pore density at the grain boundary.

From equation (12), one can derive three possible routes of interaction between a second phase particle (or pore) and a grain boundary. The first describes a process of separation of the particle from the moving grain boundary (Figure 2(a)), and this occurs when the grain boundary migration rate exceeds the particle mobility ($M_{GB}>M_p$). When the pore/particle remains attached to the grain boundary their migration rates are equal and the following two routes may occur (Figure 2(b)). When $N_z M_{GB} >> M_P$, the grain boundary mobility is limited by the particle

mobility. When $N_z M_{GB} << M_p$ the particle has no effect on the grain boundary mobility. Examining the first case, it can be seen that through this type of interaction a particle can be occluded in the grain as the grain boundary continues to migrate.

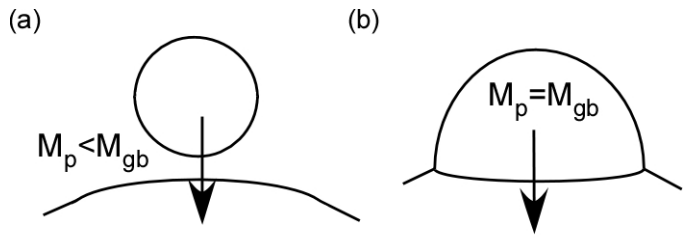

Figure 2: Schematic drawings of possible interactions between a second phase particle (or pore) and a grain boundary. (a) When the grain boundary migration rate exceeds the particle mobility ($M_{GB}>M_p$) a process of separation of the particle from the moving grain boundary occurs, and the particle eventually becomes occluded by the growing grain. (b) When $M_{GB}=M_p$ the grain boundary mobility is limited by the particle mobility.

1.4 Disconnections as the Mechanism for Grain Boundary Motion

In order to understand the influence of dopants and particles on the evolving microstructure, one must address the mechanism of grain growth first. There have been several suggestions of models that explain the mechanism for grain boundary motion [18-23]. One of the first models was Turnbull's description of a process that involves a single atom diffusing across the grain boundary, which developed as more data was accumulated, to a movement of atoms via dislocations, kinks, etc. Generally, these models can be viewed as a description of grain boundary movement caused by the motion of linear defects which can have a step and/or dislocation character, and are called disconnections [23-26]. The step component of a disconnection is attributed to be responsible for GB migration, while the dislocation component

is responsible for GB sliding. The advantage of using this approach is that it allows both microscopic and mesoscopic parameters to be addressed [24]. Gleiter used an elementary description of grain boundary movement, by describing the motion of steps at the grain boundary. He proposed that chemical changes at the GB, specifically the presence of solute atoms, changes the rate by which the step migration can occur, influencing GB mobility [27]. Han et al. calculated the energy for nucleation of a disconnection in various conditions and proposed that this energy barrier changes as solute and/or vacancies are present at the GB. In addition, Dillon et al. presented the influence of different GB complexions on mobility, which can also be described in terms of disconnections [15,24]. Therefore, the concept of atoms diffusing across the grain boundary in a random fashion has been acknowledged as being over simplistic, and a more encompassing mechanistic approach based on disconnections is now accepted.

1.5 Alumina

Aluminum oxide adopts many metastable crystallographic structures, while α-Al_2O_3 is the only structure identified to be thermodynamically stable [28]. The phase used for structural applications is in most cases rhombohedral α–Al_2O_3 [29]. This phase is referred to as corundum in its polycrystalline form and sapphire as a single crystal. For simplicity, α-alumina is usually presented using a hexagonal unit cell [30]. The production of alumina for commercial applications began in the 1930's, mainly for use as spark plug insulators [31]. The theoretical density of monolithic alumina calculated by Swanson et al. is 3.987 g/cm^3 [32]. Depending on the purity and processing method, alumina has a fracture strength (in bending) of ~300MPa, is stable at high temperatures, and has a good wear resistance [33]. These properties enable

alumina to be used for various applications in the refractory and abrasive industries. In addition, it is utilized in the fields of chemistry, mechanical and electrical engineering as a structural and functional ceramic [34]. Specific applications include bio-medical implants, reinforcing material, catalysts and abrasive materials for grinding and polishing.

As a paradigm for oxide ceramics, alumina has been the focus of study for many years. Specifically, the influence of additives and impurities on sintering, grain growth, and microstructure-dependent properties have been widely studied [35,36,37,38]. It has been shown that by adding certain dopants, polycrystalline alumina will develop different microstructures, and thus these additives can be used to engineer the manufacturing process of alumina to achieve specific properties [39,40].

In addition to the influence of dopants on the evolving microstructure of alumina, second phase particles and liquid phases can also alter sintering rates, change microstructural evolution, and directly affect the final properties [41,42]. Control over the formation of secondary phases requires knowledge of the solubility limit of key dopants and impurities at the processing temperatures [43,44]. A detailed knowledge of the solubility limit of key dopants and impurities also provides the ability to choose between microstructure control via dopants in solution (e.g. solute-drag), versus precipitates of secondary phases (e.g. Zener drag) [15,45].

1.5.1 Solid State Sintering

Sintering is the step in fabrication that provides alumina its final properties by applying thermal energy to densify the pre-compacted green body. This is usually carried out at a temperature of $0.5T_m<T<0.8T_m$ which enables sufficient atomic mobility. The densification of a green body by solid state sintering is achieved by particle shape changes and mass-transport. The driving force for densification and shrinkage of the pores during sintering is the reduction of the total surface/interfacial energy. The driving force may be expressed as [46]:

$$\Delta(\gamma A) = \Delta\gamma A + \gamma\Delta A \qquad \textbf{(13)}$$

where γ is the surface/interface energy and A is the total interface area, rendering γA as the total interfacial energy of the compacted green body. One can derive from equation (13) that the total interfacial energy (γA) may be lowered by either densification which results in a reduction of a particle interfacial energy ($\Delta\gamma$) by replacing free surfaces with grain boundaries, or by grain coarsening which results in a reduction of interface area (ΔA). Densification and coarsening are competitive processes which can occur simultaneously. If densification is the dominant process, an increase of the density as a result of pore shrinkage and eventual pore annihilation takes place. If coarsening is dominant, the particles and pores will both grow with time.

1.5.2 Grain Growth of Alumina

The most sought out enigma concerning alumina is the detailed mechanism by which MgO influences the sintering and grain growth of α-Al_2O_3. MgO inhibits pore-boundary separation, reduces discontinuous grain growth, and decreases the average grain growth rate in alumina, but the exact mechanism has yet to be understood [35]. This conundrum has received much

attention, and the motivation for solving it is clear since it will be an important step towards the ability to control and predict the sintered microstructure of alumina and other materials. Several theories were suggested to explain this phenomenon:

1. Zener drag force is introduced on the grain boundaries by second phase particles of Mg-spinel ($MgAl_2O_4$), assuming that the amount of MgO is above the solubility limit and Mg-spinel precipitation occurs.
2. A solute drag force is exerted on grain boundaries by MgO segregation to the grain boundary. The solute drag force decreases grain boundary mobility and inhibits pore separation from the boundary as well as hinders abnormal grain growth (AGG).
3. MgO segregation to the grain boundary alters the dihedral angle between pore and grain boundary, which in turn leads to a greater interaction interface area and a higher drag force on the grain boundary.
4. Pore mobility is enhanced due to MgO segregation to pore surface thus preventing pore occlusion and reducing grain boundary mobility.

Observations of the same MgO effect were detected in single and pore free alumina thus rendering theories 1 and 4 as obsolete [40]. It is currently commonly accepted that the decrease in grain boundary mobility in MgO doped alumina stems from a solute drag effect [5].

The degree to which Al_2O_3 responds to MgO doping has evidently been dependent on the composition and concentration of background impurities and particulates in the alumina matrix. Handwerker et al. showed that when introducing common impurities such as CaO and SiO_2, MgO eliminates second phase formation and reduces impurity concentration at the grain boundary [35]. A relationship between MgO doping and Si segregation to the grain boundaries suggests that a proper ratio between the cations must be achieved in order to obtain a dense microstructure. Furthermore, these results suggest that a co-doping effect is involved, and that MgO reduces the solubility limit of impurities. In nanocomposites, it has been shown that MgO

plays a substantial role in the location of Ni nanoparticles in alumina. Gluzer et al. demonstrated MgO segregation to the Ni-alumina interface and correlated it with the promotion of particle occlusion [47].

Dillon et al. studied grain growth kinetics in alumina doped with CaO or with SiO_2 in a broad range of sintering temperatures. This investigation was done to unravel the contradicting results of earlier studies regarding AGG in doped alumina [15,48]. Some studies showed the presence of intergranular films associated with AGG, others claimed that AGG is due to grain boundary faceting or the lack of it, while others attributed exaggerated growth to the shape of the grain (equiaxed or elongated) [49,50-52]. Dillon and Harmer correlated different grain boundary mobilities to "six" different complexions [48]. Each complexion was defined by its apparent thickness attained from high resolution scanning transmission electron microscopy (HRSTEM), without directly discerning the grain boundary structure or the amount of solute at the boundary. The concept of only "six" complexions was based on STEM observations, and is not founded in thermodynamics, and there is no real limit to the number of complexion transitions as a function of dopant concentration and temperature. The limited number of transitions found by Dillon et al. may stem from the specific temperature range used, in which a relatively small number of grain boundary structures and chemistries are dominant [9]. More likely, classification by "width" alone, ignoring structure and chemical content, is probably an incorrect approach.

Be that as it may, from Dillon and Harmer's study one can observe that the mobility of CaO doped samples is greater than that of undoped samples. This result questions the validity of the

of solute drag theory. In their work, Dillon and Harmer attributed this behavior to a complexion transition. Each transition was regarded with a different mobility and was (indirectly) correlated to the amount of CaO excess at the grain boundary, which in turn alters the structure and chemistry of the boundary. Despite the importance of dopant excess at the grain boundary for the conclusions derived from this study, an actual *measurement* of the excess was not carried out (or presented). Furthermore, the amounts of dopant used were above the solubility limit, but no actual characterization of the amount of dopant content in the samples was done, nor was the presence of a second phase eliminated.

Akiva et al. conducted mobility measurements of CaO or MgO doped alumina samples with dopant levels measured in the actual final material [11]. They showed that below the solubility limit, both MgO and CaO adhered to their well-known behavior and exhibited reduced and enhanced grain boundary mobility, respectively. This confirmed that the influence of CaO was via adsorption, and not by the formation of a liquid phase. In addition, excess measurements between the basal plane of sapphire and polycrystalline CaO doped alumina showed the presence of CaO at the interface, proving the occurrence of Gibbsian segregation.

The presence of complexions and their influence on the evolving microstructure of nanocomposites based on alumina was investigated by Avishai et al. [53]. Ni reinforced alumina nanocomposites were doped with CaO or SiO_2 and occlusion of the metal particles was observed, whereas undoped samples did not present an occluded particle microstructure. In the doped samples, the presence of an intergranular film (IGF) was confirmed and attributed to an increase in grain boundary mobility. However, it should be noted that doping levels in

this study were above measured solubility limits for both CaO and SiO_2, leading to the formation of anorthite glass at the triple junctions, which no doubt had an effect on the triple junction mobility [54].

2. Research Goals

The development and fabrication of polycrystalline ceramics as well as nanocomposites is still, to this day, mainly based on a "cook & look" (trial and error) approach. Studies have investigated the influence of solute and particle content on grain boundary mobility in alumina. However, a correlation between these factors at dopant levels below the solubility limit is missing from the literature. This is required to fundamentally understand the evolving microstructure. This is important, since it is known that even in high purity ceramic powders, trace levels of dopants are found which can have a major influence on the final microstructure. In addition, while theoretical models that explain a microstructure as a function of process variables have been developed, to the best of our knowledge, a correlation between theoretical models and experimental data has yet to be explored for ceramic matrix nanocomposites with regards to the influence of impurities in the matrix.

The main goal of this research is to study the influence of impurities, at concentrations below the solubility limit, on the evolving microstructure of alumina and alumina reinforced with sub-micron particles of Ni. The fundamental hypothesis is that the solute drag theory, and the underlining theories for grain boundary migration are overly simplistic. The mechanism for grain boundary movement by disconnection motion is, alternatively, a more complete approach that can also explain the influence of solute on GB mobility (accelerating and hindering). Exploring this experimentally will enhance our understanding regarding the impact of solutes and impurities on the final microstructure of alumina.

3. Experimental Methods

The experimental methods described below were employed in this study to reach a fundamental understanding of the influence of impurities on the evolving microstructure of a ceramic material, specifically alumina and Ni-alumina nanocomposites. In this section alumina processing routes, characterization methods and methodology will be presented. The impurity levels added to the matrix were measured post-processing to establish dopant levels below the solubility limit and to allow investigation of the evolving microstructure affected by impurity segregation to the metal ceramic interface, *without* the presence of impurity second phase particles. The experiments were chosen to explore grain boundary acceleration, grain boundaries retarded by Zener drag, and a combination of both. This was achieved by the investigation of monolithic CaO doped alumina and CaO doped Ni-alumina. Each system was studied at various dopant levels. For a kinetic understanding, the effective mobility was measured as a function of measured dopant level. The influence of dopants on occlusion rate was also studied.

In addition, the solubility limits of SiO_2 and MgO combined with CaO in alumina were determined to provide key information on the levels of solute that will change the mechanism of grain boundary motion from controlled by solute (solute drag or acceleration) to controlled by particles (Zener drag).

In addition, the influence of Cr_2O_3 and MgO combined doping on the microstructural evolution of Ni-alumina, specifically on particle location, was examined.

3.1 Alumina Processing

Obtaining knowledge of the solubility limits of dopants and impurities in alumina, and the actual value of dopant concentration after processing is essential to correctly analyze and understand grain boundary mobility data. In this study, the solubility limit of SiO_2 in alumina as well as the solubility limit of alumina co-doped with CaO and MgO were determined according to the method described by Miller et al. [43]. These values were to be added to the accumulated knowledge of the solubility limit of CaO in alumina and MgO in alumina previously, determined using the same methodology [43,44].

The solute drag theory was studied by examining the influence of Ca on grain boundary mobility, at concentrations below the solubility limit in alumina and Ni-alumina. To do so, alumina and Ni-alumina samples were doped with various Ca concentrations which were determined to be below the Ca solubility limit, and mobility measurements were conducted. The mobility trend shows an increasing grain boundary mobility as a function of *increasing* Ca concentration. Thus, the presence of Ca in alumina and Ni-alumina has an accelerating effect, which increases with increasing Ca concentration, indicating the absence of a solute drag force due to Ca segregation.

3.1.1 Solubility Limits of Dopants in Alumina at 1600°C

Polycrystalline alumina samples were prepared using high purity α-Al_2O_3 powder to which a concentration of solute that was above the solubility limit was added. Subsequent to powder preparation, green samples were prepared and were sintered at temperatures high enough to facilitate secondary phase formation, and then annealed at 1600°C. Sintering and annealing conditions were chosen to achieve large alumina grains to facilitate the measurement of solutes in solution, and to provide sufficient time for diffusion of solutes to reach equilibrium. Annealing was followed by quenching in water. Samples served for subsequent wavelength dispersive spectroscopy (WDS) measurements to determine the solubility limits of SiO_2 in alumina and of CaO and MgO combined in alumina at 1600°C. Scanning electron microscopy (SEM) specimens for WDS measurements were prepared by cutting and mechanically polishing interior sections of each sample. No chemical or thermal etching was performed on the samples used for WDS to prevent possible changes in concentration.

3.1.1.1 SiO_2 in Alumina

Polycrystalline alumina samples were prepared using high purity (99.99%) α-Al_2O_3 powder (Ceralox HPA 0.5, Tucson, Arizona), to which 6 wt.% of fumed silica powder (Sigma-Aldrich S5130, St. Louis, Missouri) was added. The powder mixture was used to form green bodies by dry pressing at 20 MPa, followed by cold isostatic pressing (CIP) at 27 MPa. The samples were sintered at 1700°C for 40 hours in air (heating/cooling rates of 10°C/min). Once sintered, this resulted in the presence of only mullite ($3Al_2O_3 \cdot 2\ SiO_2$) and alumina grains. The equilibrated two-phase sample necessarily means that the alumina grains are saturated with Si. An additional 24 hours of annealing at 1600°C in air was conducted, followed by quenching in

water (cooling rate ~200°C/s). These samples served for WDS measurements to determine the Si solubility limit in alumina at 1600°C. Additional samples were furnace-cooled (cooling rate of 10°C/min).

3.1.1.2 Alumina Co-Doped with MgO and CaO

Using the same methodology, samples were prepared using the same high purity (99.99%) α-Al_2O_3 powder mentioned above, to which a water solution containing 5 wt.% of calcium nitrate ($Ca(NO_3)_2 \cdot 4H_2O$, (Carlo Erba Reagents, Italy)) and 10 wt.% magnesium nitrate ($Mg(NO_3)_2 \cdot 6H_2O$, (Merck KGaA, Germany)) was added. Deflocculation of the alumina suspensions was conducted by adding a small amount of analytically pure HCl to reach a pH of ~4. Mixing was performed for 24 hours using a ball-milling system, without milling balls to reduce contamination. To produce the ceramic preforms, suspensions were slip cast and dried in air at room temperature for 36 hours and then dried in air at 110°C for 5 hours. Once the samples were dry they were crushed using a mortar and a pestle. Green bodies were prepared using a uniaxial press at 14 MPa. The green bodies were sintered at 1600°C for 48 hours (heating/cooling rate 10°C/min). This resulted in the formation of $MgAl_2O_4$ (Mg spinel), $CaO \cdot 6Al_2O_3$ (CA6), a ternary phase $Ca_2Mg_2Al_{28}O_{46}$ (CAM-II) and alumina grains. The presence of these equilibrated phases in the sample necessarily means that the alumina grains are saturated with Mg and Ca. An additional 10 hours of equilibration at 1600°C in air was followed by quenching in water (cooling rate ~200°C/s). These samples served for subsequent WDS measurements to determine the Mg and Ca co-doping solubility limit in alumina at 1600°C.

3.1.2 Grain Boundary Mobility in Ca Doped Alumina

Polycrystalline alumina samples were prepared using the same alumina powder mentioned above, to which water and calcium nitrate ($Ca(NO_3)_2 \cdot 4H_2O$) were added. The amount of calcium nitrate added was varied to reach expected concentrations of 10, 20 and 40 ppm of calcium in the alumina. In addition, a sample was prepared without calcium nitrate to produce an undoped sample for comparison with the Ca-doped samples. Deflocculation of the alumina suspensions was conducted by adding a small amount of analytically pure HCl to reach a pH of ~4. Mixing was performed for 72 hours using a ball-milling system, without milling balls to reduce contamination. To produce the ceramic preforms, suspensions were dried in air at 60°C for 24 hours and were crushed using a mortar and a pestle. Green bodies were prepared using a uniaxial press at 14 MPa followed by CIP at 207 MPa. The green bodies were bisque-fired at 850°C for 2 hours in air (heating rate 10°C/min) and then sintered at 1600°C for 2 hours (heating rate 10°C/min) in a high-temperature resistance furnace (Thermal Technology Inc, Model 1000) with graphite heating elements and crucibles under flowing He (99.995%).

After sintering, specimens for SEM and WDS measurements were prepared by slicing and then mechanical polishing of the interior sections of each sample. No chemical or thermal etching was performed on the samples used for WDS to prevent possible changes in concentration. Once the Ca concentration was determined samples were annealed for 1 min, 5 hours, or 10 hours at 1600°C under flowing He. Relatively short annealing times were used, since Akiva et al. showed that anisotropic growth occurred after ~20 hours of annealing at 1600°C, and anisotropic grains require a more complicated approach to determine the grain boundary mobility [11]. For grain size measurements after thermal annealing, thermal etching was

conducted at 1250°C for 3 hours. The grain size was determined using the linear intercept method [55]. A correction factor of 1.56 was used. Grain size was determined from measuring more than 600 grains in each sample [3].

3.1.3 Grain Boundary Mobility in Ni-Alumina Composites

Ni-alumina samples were fabricated using the same process as samples prepared for measuring the mobility in Ca-doped alumina (see section 3.1.2). Once samples were bisque-fired a nitrate solution was infiltrated to introduce Ni to the alumina preforms and form the composite.

During the infiltration process the fired green bodies were placed in a beaker with a water based Ni nitrate solution (30 wt.% $Ni(NO_3)\cdot 6H_2O$) and placed in a vacuum desiccator (10^{-3} torr) for ~5 hours. After 5 hours the beakers were removed from the vacuum desiccator and placed in an air furnace for 2 hours at 60°C, to reduce the contact angle of the Ni nitrate on alumina and promote infiltration [56]. The Ni nitrate was removed from the beakers and the samples were dried for 12 hours at 25°C in air and then additionally, for 5 hours at 110°C in air. Once dried, the samples were reduced to form Ni particles in flowing forming gas (93% Ar 7% H_2) at 600°C for 2 hours. The infiltration and reduction processes were performed once more to increase the amount of nickel in the alumina to ~3 wt.% Ni [57]. Infiltrated alumina samples were then sintered at 1600°C for 2 hours (heating rate 10°C/min) in a high-temperature resistance furnace (Thermal Technology Inc, Model 1000) with graphite heating elements and crucibles under flowing He (99.995%), as done for Ca-doped alumina samples described above (section 3.1.2). The same procedure was used in order to compare between the Ni-alumina composites to the alumina samples. Sample preparation for SEM, WDS and grain size mobility measurements were also conducted in the same manner.

3.1.4 The Influence of Dopants on Ni Occlusion in Ni-Alumina Composites

Alumina water-based slips were prepared by using high purity alumina powder to which a water solution containing 1 wt.% of MgO was added. This resulted in a Mg content in the alumina grains which was below the solubility limit [43]. Chromium nitrate was added to reach ~1wt.% Cr_2O_3, as well as analytically pure HCl to reach a pH of ~4. The slips were mixed for 24 hours using a ball-milling system. Green bodies were formed by slip casting followed by CIP at 27 MPa. The samples were then infiltrated with Ni nitrate solution and underwent heat treatment as described in the previous section. Infiltrated green bodies were then sintered in He at 1600°C for 4 hours to result in Ni-alumina samples which were doped with both MgO and Cr_2O_3.

3.2 Characterization

3.2.1 X-Ray Diffraction and Energy Dispersive Spectroscopy

X-ray diffraction (XRD) was used to conduct phase analysis. XRD patterns were acquired using a conventional X-ray powder diffractometer (Rigaku MiniFlex) with a Cu Kα tube, operated at 15mA and 30 kV, with 0.3 mm receiving slits. Diffraction patterns were acquired at steps of $2\theta = 0.01°$ and 1.2 sec per step exposure. Energy dispersive spectroscopy (Link Isis, Oxford Instruments) was also used to confirm the presence of secondary phases in the SEM samples.

3.2.2 TEM and HRS/TEM-EDS

Further investigation of the phases and determination of particle occlusion was conducted by transmission electron microscopy (TEM, Tecnai T-20 G2 200kV, FEI, Eindhoven, Holland) and elemental analysis was done by scanning transmission electron microscopy (STEM) and energy dispersive spectroscopy (EDS, EDAX, Tilburg, Holland) to corroborate the XRD results.

High resolution scanning transmission electron microscopy (HRSTEM) was conducted using a monochromated and double-corrected S/TEM (Titan-Themis^3 300, FEI) to acquire micrographs. EDS measurements were acquired using an FEI Super-X detector system mounted on the Titan.

3.2.3 WDS

The solute concentrations were measured using WDS (Oxford Instruments, High Wycombe, U.K.) mounted on a scanning electron microscope (FEI E-SEM Quanta 200, Eindhoven, Holland). WDS measurements were acquired from sectioned samples which were coated with carbon to prevent charging under the electron beam. To optimize for a signal to background intensity ratio, an accelerating voltage of 20 kV, 20 kV and 30 kV was used for Mg, Si and Ca concentration measurements, respectively. A polyethylene terephthalate crystal was used as a monochromator for WDS. Diopside ($CaMg(Si_2O_6)$) was used as a standard for Mg and Ca. Over 300 measurements were conducted at random locations across the cross-section of each sample, avoiding areas that were identified from SEM as being secondary phases (Mg spinel,

CA6, CAM-II or mullite), and data analysis was executed according to the method developed by Miller et al. [43].

The WDS measurements were conducted at operating conditions described by Akiva et al. [44]. The limit of detection was determined using [58,59]:

$$\mathbf{C_{lim,0.975} = g_{ZAF} \cdot C_{std} \cdot \frac{2\sqrt{2I_{bg}}}{\sqrt{m\tau} \cdot I_{std}}} \quad [14]$$

where $C_{lim,0.975}$ is the limit of detection with a confidence probability of 97.5%. The XPHI software was used to calculate the g_{ZAF} correction factor [60]. I_{bg} is the background intensity; C_{std} and I_{std} are the concentration and intensity from a standard with a known concentration, respectively, m is the number of measurements, and τ is the measurement time.

4. Results

4.1 Solubility Limits of Dopants in Alumina at 1600°C

4.1.1 SiO_2 in Alumina

XRD data for a Si saturated Al_2O_3 sample that was furnace cooled from 1600°C is presented in Figure 3. The XRD pattern confirms the presence of only mullite ($3Al_2O_3 \cdot 2SiO_2$) and alumina. Figure 4 presents a backscattered electron (BSE) SEM micrograph from a cross-section of the same sample that underwent thermal etching. The microstructure indicates that liquid-phase sintering occurred until the SiO_2 reacted with alumina to form crystalline mullite (see arrow in Figure 4). EDS (from the region indicated with an arrow in Figure 4) corroborates the XRD findings (see Table 1).

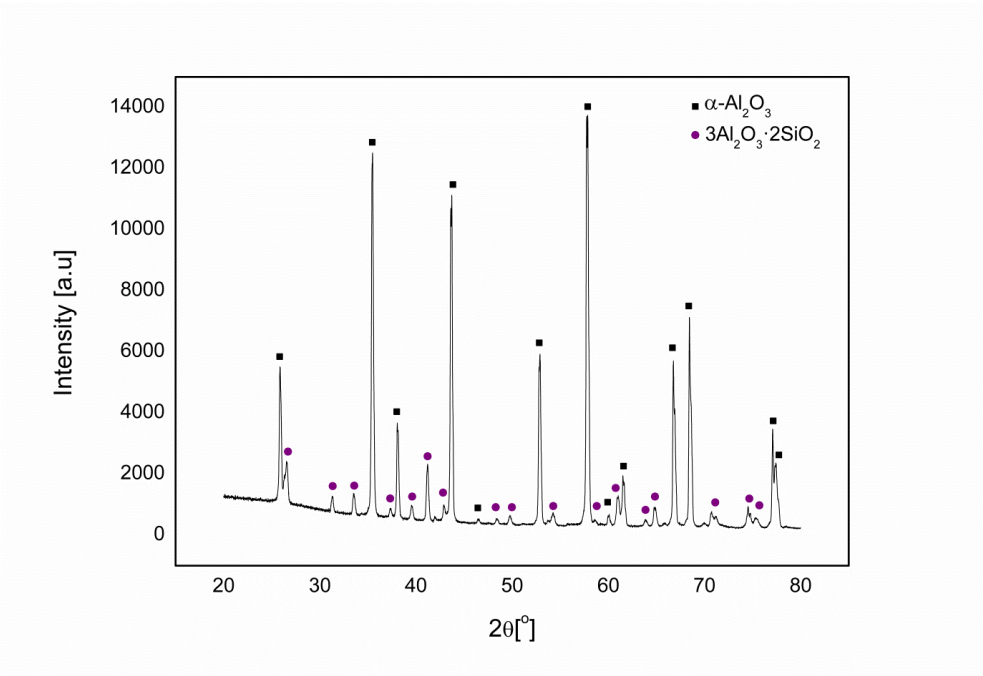

Figure 3: XRD pattern confirming the presence of only mullite ($3Al_2O_3 \cdot 2SiO_2$) and alumina, thus ensuring saturation of the alumina grains with Si.

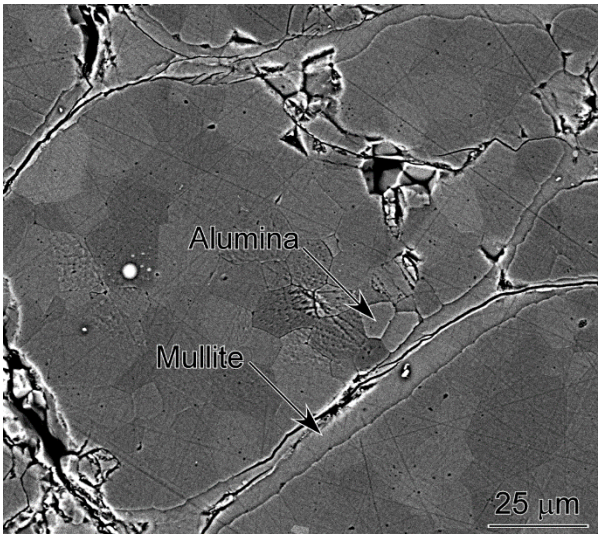

Figure 4: BSE SEM micrograph of an alumina sample doped with SiO_2, which underwent liquid phase sintering until the SiO_2 reacted with alumina to form crystalline mullite.

Table 1: EDS measurement from a mullite grain detected in the quenched sample (see arrow in Figure 4), confirming the XRD results that a two phase system formed.

Element	Measured Concentration [at.%]	Stoichiometric Concentration [at.%]
O	68.8	69
Al	23.6	23.25
Si	7.6	7.75

Figure 5 displays a bimodal distribution histogram of the measurement frequency versus Si concentration. This histogram may be divided into two regions after fitting to a Gaussian distribution (indicated with a red line). Following the approach developed by Miller et al. [43], the peak at 212±5 ppm correlates to the Si concentration within the alumina grains and thus is the solubility limit of Si in alumina at 1600°C. Considering the WDS/SEM operating conditions and the number of measurements conducted for each sample (>300), the limits of

detection for Mg, Ca and Si were determined to be 11 ppm, 1 ppm and 3 ppm, respectively. Using the same method, the Si content in alumina grains from samples that were furnace cooled from 1600°C at a rate of 10°C/min was measured and found to be 154±4 ppm. As expected, the Si content of the furnace cooled samples was significantly lower than that of the quenched samples, indicating a solubility limit for a temperature below 1600°C but before Si diffusion becomes insignificant.

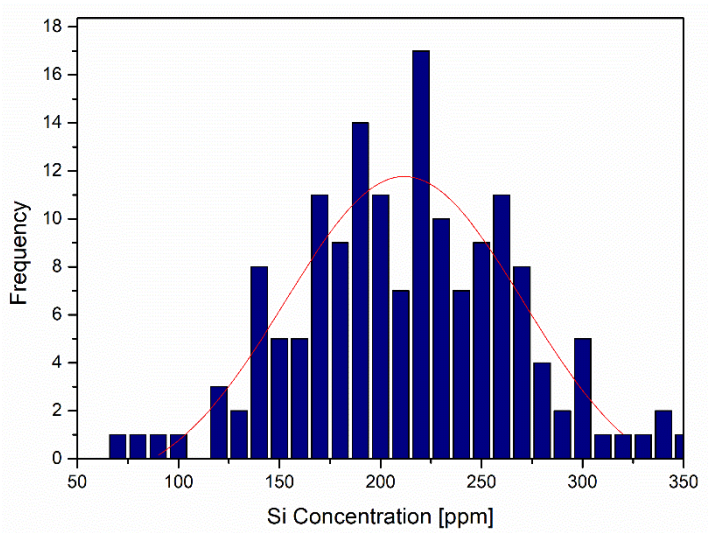

Figure 5: Histogram of the Si concentration measurements from the specimens quenched from 1600°C.

4.1.2 Alumina Co-Doped with MgO and CaO

Figure 6 presents an XRD pattern acquired from a Mg and Ca saturated alumina sample that was quenched in water from 1600°C. The reflections in the XRD data confirm the presence of $MgAl_2O_4$ (Mg spinel), $CaO_6Al_2O_3$ (CA6) and $Ca_2Mg_2Al_{28}O_{46}$ (CAM-II), in addition to alumina. The presence of the secondary phases necessarily means that the alumina grains are saturated (at the solubility limit) with Ca and Mg.

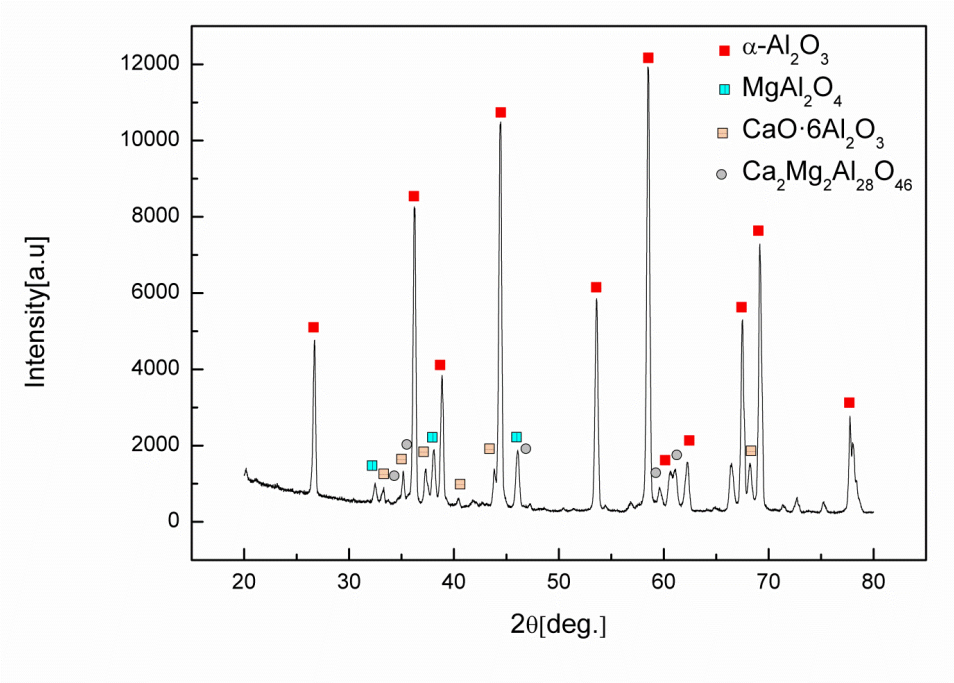

Figure 6: XRD pattern confirming the presence of alumina, and binary and ternary phases, thus ensuring saturation of the alumina grains with Mg and Ca.

Figure 7 presents a backscattered electron (BSE) SEM micrograph from a cross-section of a Mg and Ca saturated alumina sample, which underwent sintering until the CaO and MgO reacted with alumina to form crystalline CAM-II. The sample was thermally etched (1350°C for 3 hours) in order to provide contrast for SEM characterization of the microstructure. The regions with light contrast were identified by EDS to be CAM-II. Also evident are regions with dark contrast that are residual pores in the alumina matrix. Figure 8 presents a bright field TEM micrograph of a CAM-II grain in the quenched sample. EDS measurements in TEM confirmed the existence of CAM-II (see Table 2).

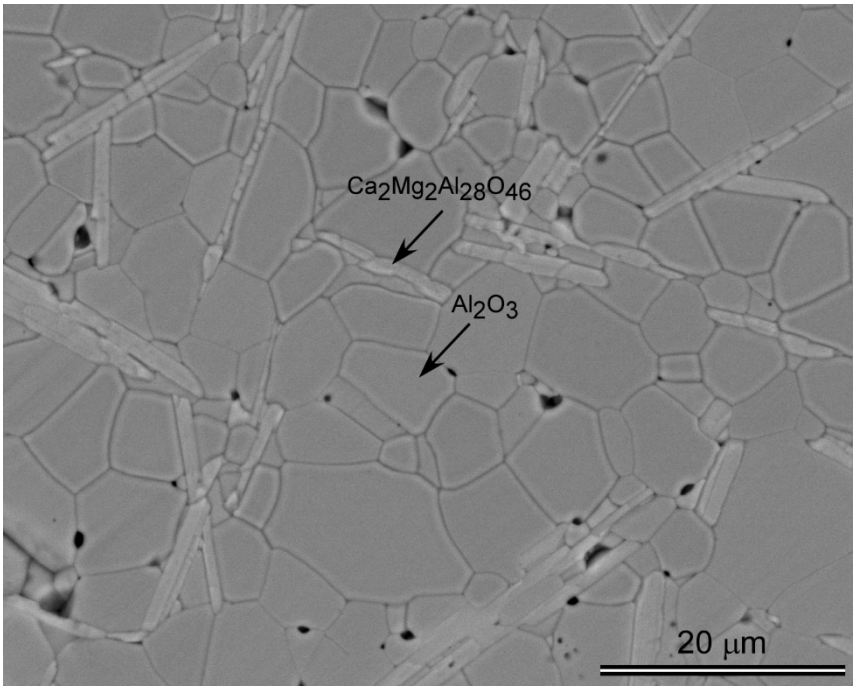

Figure 7: BSE SEM micrograph of an alumina sample doped with CaO and MgO, which underwent sintering until the CaO and MgO reacted with alumina to form crystalline CAM-II.

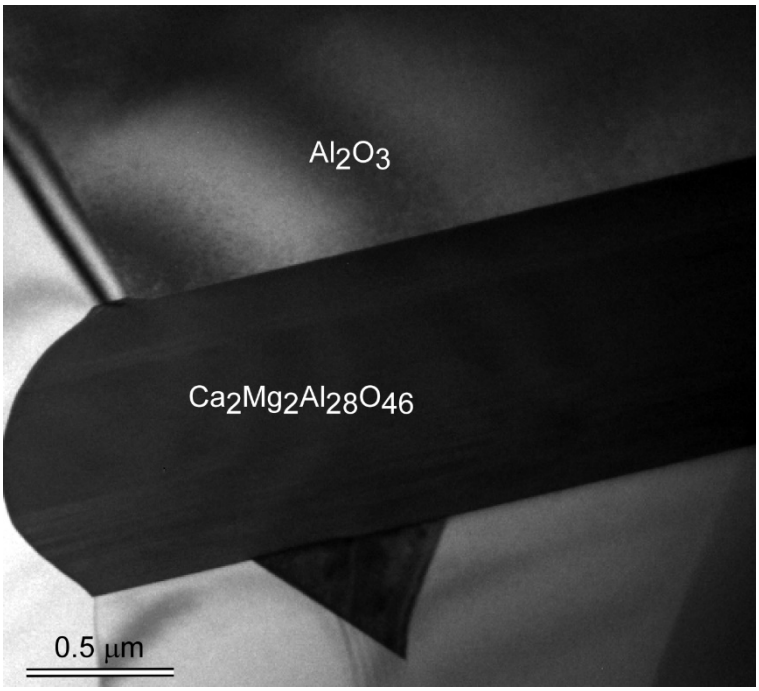

Figure 8: Bright field TEM micrograph of a CAM-II precipitate.

Table 2: EDS measurement from a CAM-II grain detected in the quenched sample (as shown in Figure 8), confirming the XRD results that the ternary $Ca_2Mg_2Al_{28}O_{46}$ phase formed.

Element	Measured Concentration [wt.%]	Theoretical Stoichiometric Concentration [wt.%]
O	45.7	45.4
Mg	2.7	3
Al	46.6	46.6
Ca	5	5

Histograms of the measurement frequency versus the measured cation concentration are presented in Figure 9 for Ca and in Figure 10 for Mg. Following the method developed by Miller et al. [43], the histograms were used to determine the concentrations of Ca and Mg in the saturated alumina grains. The peak at 32±13 ppm of Ca in Figure 9 and the peak at 210±43 ppm of Mg in Figure 10 were determined as the solubility limit of these cations in alumina co-doped with Ca and Mg at 1600°C. These values are well above the limit of detection for the cations, which was determined to be 1 ppm and 11 ppm, for Ca and Mg respectively.

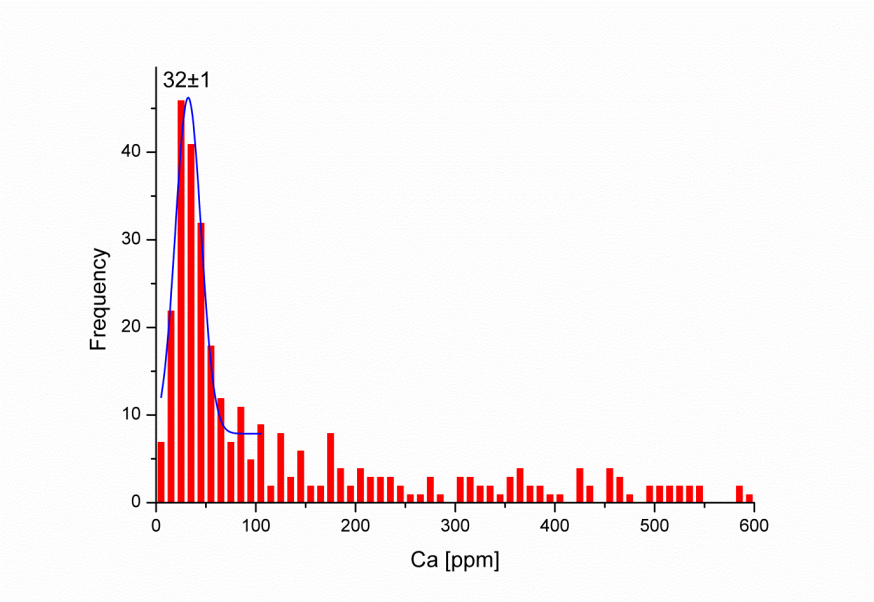

Figure 9: Histogram of the Ca concentration measurements from the specimens quenched from 1600°C.

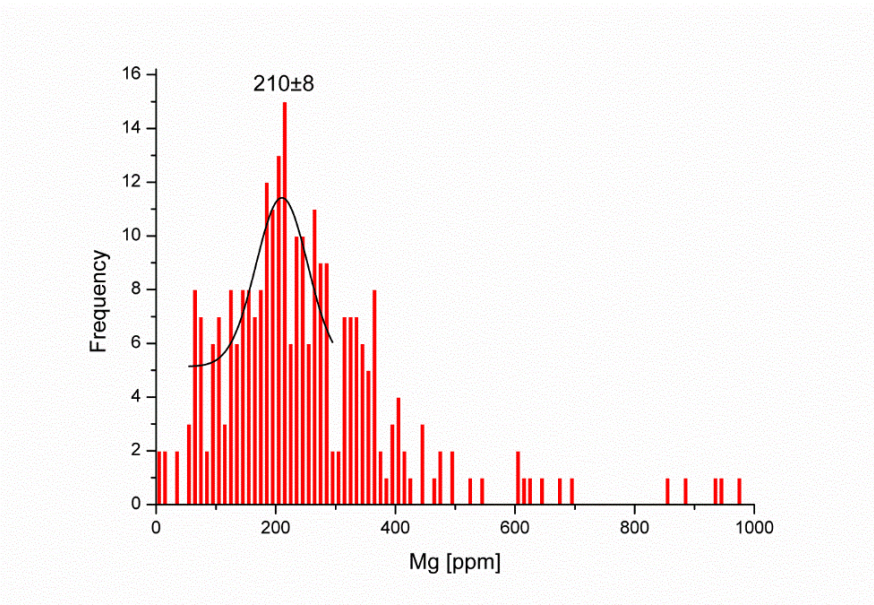

Figure 10: Histogram of the Mg concentration measurements from the specimens quenched from 1600°C.

4.2 Grain Boundary Mobility in Ca Doped Alumina

4.2.1 Chemical Characterization

XRD data of an alumina sample doped with 40 ppm of calcium is presented in Figure 11. The XRD pattern presents no detectable secondary phases, although the expected detection limit for conventional XRD would probably be insufficient to detect $CaO_6Al_2O_3$ at dopant levels immediately above the detection limit.

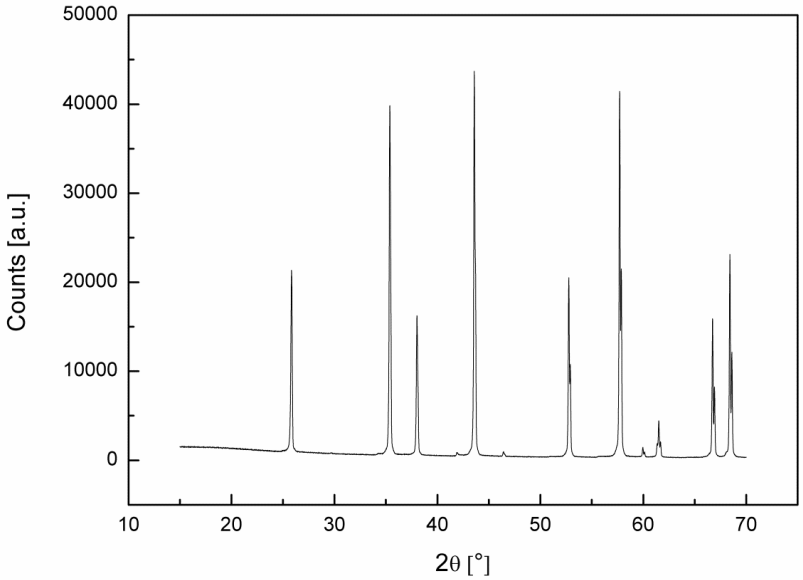

Figure 11: XRD pattern of alumina doped with 47 ppm of CaO, showing only reflections from α-Al_2O_3, i.e. no reflections from $CaO_6Al_2O_3$ (CA6) are detectable.

Figure 12 presents a histogram of the Ca concentration that was measured using WDS for the doped and undoped alumina samples. A summary of the results is given in Table 3. WDS measurements confirmed the calcium concentration to be below the solubility limit for each sample [43,44]. Determining the actual dopant concentration by WDS was done to be able to

firmly correlate the morphological changes with the *actual* Ca content in the sample, and not based on the initial amount of dopant added to the powders. As can be seen from the results summarized in Table 3. The amount of dopant in the sintered material can change during processing, probably depending on the drying process for the water-based doping method and/or the dopant's vapor pressure.

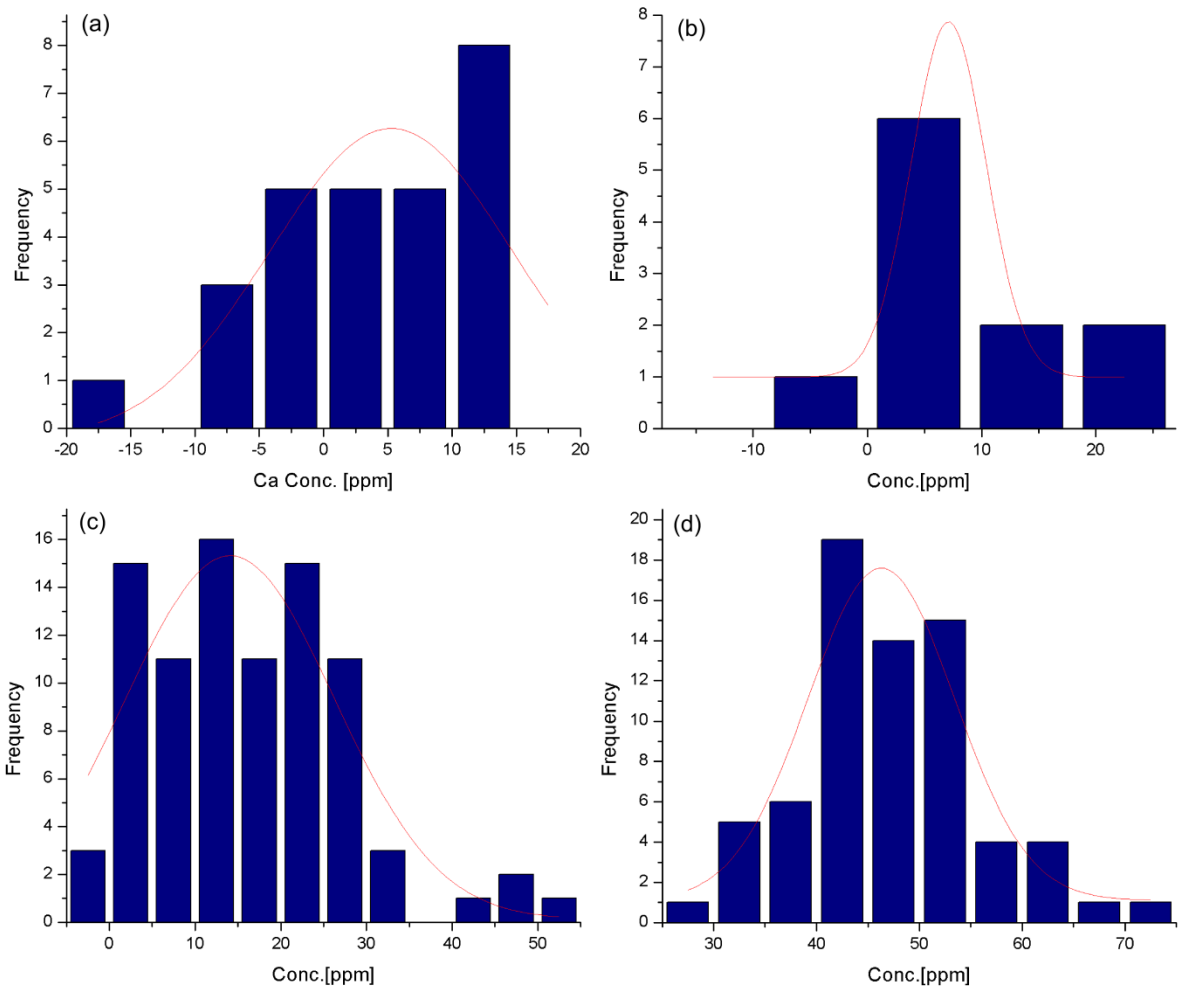

Figure 12: Histograms of Ca concentration measurements from undoped and doped specimens sintered at 1600°C for 2 h in He: (a) trace (3±1 ppm) of Ca in the undoped sample; (b) 9±1 ppm of Ca in doped alumina; (c) 15±2 ppm of Ca in doped alumina; (d) 47±1 ppm of Ca in a doped alumina.

Table 3: WDS measurements from alumina doped with various amounts of Ca, which was used to determine the actual Ca concentration of each sample.

Amount of Dopant Added	Measured Ca Content [ppm]	Limit of Detection [ppm]
Un-Doped	3±1	3
10 ppm Ca	9±1	5
20 ppm Ca	15±2	2
40 ppm Ca	47±1	1

Elemental analysis was conducted on Ca doped samples using HRSTEM and EDS to characterize Ca GB segregation as a function of sample Ca doping. Figure 13 displays representative HRSTEM micrograph of an alumina grain boundary that was chemically characterized by EDS. Figure 14 presents EDS mapping of an alumina GB in a sample doped with 47 ppm of Ca, with a Ca excess at the GB (Figure 14(c)). The Ca excess was measured using the spatial difference method and calculated according to [44,61,62,63]:

$$\Gamma_{Ca} = \frac{V}{S} \cdot \rho_{Al_2O_3} \cdot k_{Ca/Al} \cdot \frac{2A_{Al}}{A_{Ca}} \cdot \frac{I_{Ca}}{I_{Al}} \qquad [15]$$

where V/S is the ratio between the interaction volume and the area of the GB inside the interaction volume. $\rho_{Al_2O_3}$ is the alumina density in atoms/nm^3, A_{Al}, A_{Ca}, I_{Al} and I_{Ca} are the atomic masses and the measured intensities of Al and Ca, respectively. $k_{Ca/Al}$ is the factor referring to the Z correction between the X-ray intensities for the standard and the studied specimen for Ca in alumina. A correction factor of 0.9±0.13 was used [44].

The intensity at the grain boundary is determined by [62]:

$$I_{Ca} = I_{Ca}^{GB} - \frac{1}{2}\left(I_{Ca}^{grain\ A} + I_{Ca}^{grain\ B}\right) \quad [16]$$

where I_{Ca}^{GB} is the intensity of Ca measured at the area containing the GB, and $I_{Ca}^{grain\ A}$ and $I_{Ca}^{grain\ B}$ are the intensities of Ca measured from the adjacent grain A and grain B, receptively. The limit of detection is calculated using [44,61]:

$$\Gamma_{min} = \frac{V}{S} \cdot \rho \cdot k_{Ca/Al} \frac{2 \cdot A_{Al}}{A_{Ca}} \frac{\sqrt{2 \cdot I_{Ca}^{b}}}{I_{Al}} \quad [17]$$

where I_{Ca}^{b} is the intensity of the background under the peak of interest.

Three EDS measurements with the same measurement area, were conducted to determine the excess of Ca at the GB. One at the GB and two at adjacent grains. After subtracting the Ca signal coming from the GBs, the excess of Ca was determined as summarized in Table 4.

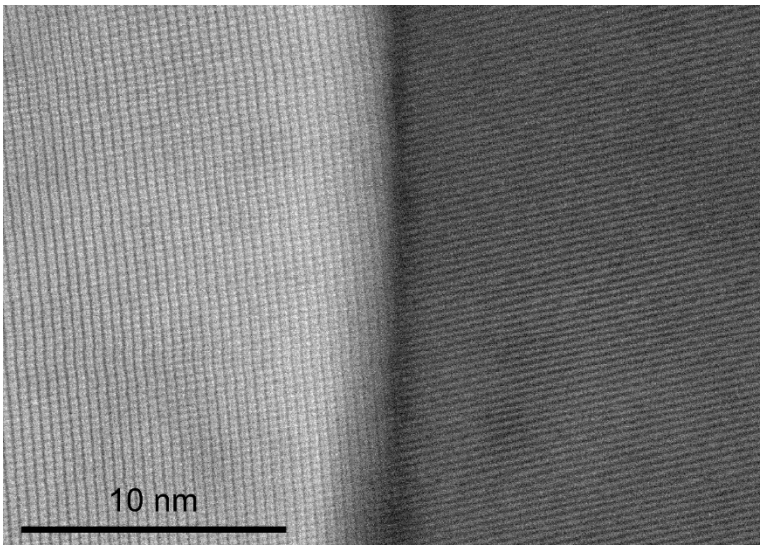

Figure 13: HRSTEM micrograph of a GB in alumina doped with 47±1 ppm of Ca.

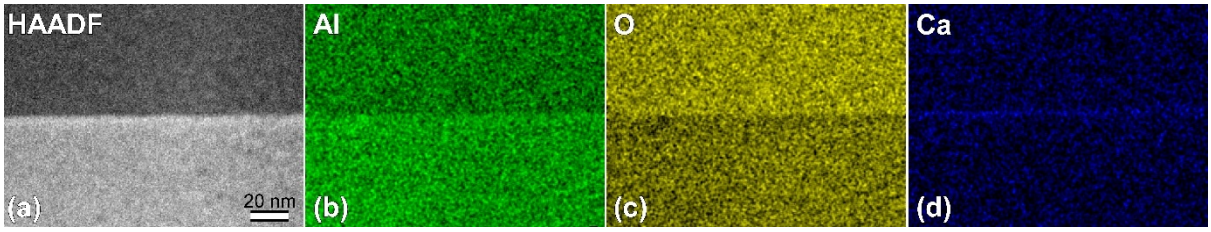

Figure 14: (a) HAADF-STEM micrograph of alumina GB in alumina sample doped with 47 ppm of Ca. (b)-(d) EDS elemental map of Al, O and Ca acquired simultaneously with the micrograph presented in (a).

Table 4: Ca concentration determined by WDS measurements and Ca GB excess measurements.

Ca Concentration [ppm]	Ca Grain Boundary Excess [atoms/nm^2]	Limit of Detection [atoms/nm^2]
15±5 CaO	<0.07	0.07
47±1 CaO	0.18±0.05	0.07
Above the solubility limit (Sample co-doped with Mg & Ca)	2.2±0.2	0.6

4.2.2 Mobility Measurements

Figure 15 shows a representative backscattered electron (BSE) SEM micrograph from a cross-section of an alumina sample doped with 47 ppm of Ca and annealed at 1600°C for 10 hours. Prior to SEM, the sample was thermally etched at 1250°C for 3 hours. The micrograph exhibits an equi-axed microstructure, as expected for early stages of Ca doped alumina grain growth. To conduct grain growth analyses using the parabolic behavior, thermal annealing was carried out for 1 minute, 5 hours or 10 hours [11]. The grain boundary mobility as a function of calcium concentration is shown in Figure 16, displaying faster grain growth with an increase

in dopant (Ca) concentration (at concentrations confirmed to be below the solubility limit). This trend discontinued for samples doped with 47 ppm of Ca, which is a dopant level that approaches the solubility limit (51 ppm of Ca at 1600°C [44]).

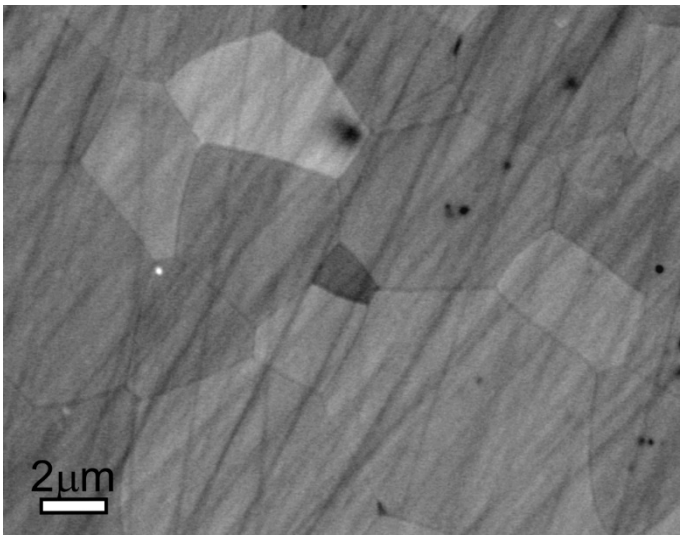

Figure 15: BSE SEM micrograph of the microstructure of alumina doped with 47ppm Ca and annealed at 1600°C for 10 hours.

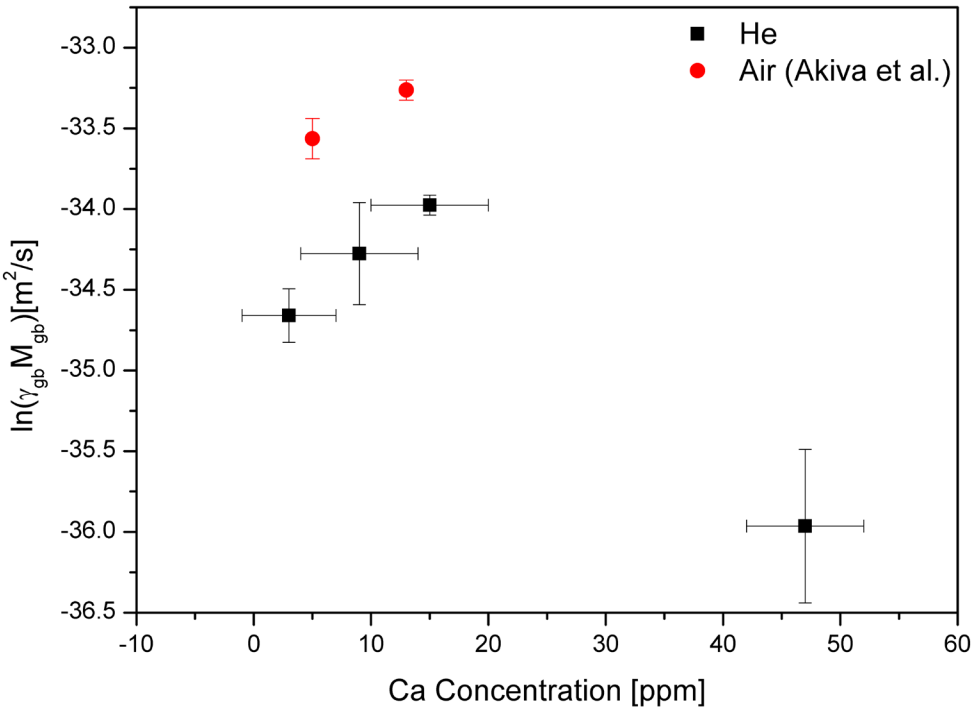

Figure 16: Effective grain boundary mobility of undoped alumina and alumina doped with 9, 15 and 47 ppm of Ca, annealed at 1600°C in He (marked ■), compared with the effective grain boundary mobility of undoped alumina and alumina doped with 13 ppm of Ca determined by Akiva et al. (marked ●) [11].

4.3 Grain Boundary Mobility in Ni-Alumina Composites

4.3.1 Chemical Characterization

WDS measurements conducted on samples (two batches) that were infiltrated with Ni particles were determined to have a solute concentration of 5 ppm of Ca and 18 ppm of Ca. Once the Ca concentration was confirmed to be below the solubility limit, mobility analysis was carried out [43,44].

4.3.2 Mobility Measurements

A representative backscattered electron (BSE) HRSEM micrograph from a cross-section of an alumina sample doped with 5 ppm of Ca is given in Figure 17. The micrograph exhibits equi-axed alumina grains and homogenously dispersed Ni particles in the microstructure. To conduct grain growth analyses using the parabolic behavior, thermal annealing was carried out for 1 minute, 5 hours or 10 hours [11]. The grain size of Ca doped alumina and Ca doped Ni-alumina as a function of annealing time is shown in Figure 18. The grain boundary mobility as a function of calcium concentration is shown in Figure 19, demonstrating the influence of the Zener drag force induced alumina grain boundaries by the presence of Ni particles. Analytical EDS STEM tomography was conducted to study the drag influence Ni particles exert on alumina GB. A representative micrograph is given in Figure 20, showing the curved facets of the Ni particles being dragged by the GBs. In addition, the grain size as a function of time of undoped Ni-alumina compared to Ni-alumina doped with 18 ppm of Ca is presented in Figure 21, displaying faster grain growth with an increase in dopant (Ca) concentration, validating the accelerating influence of Ca on alumina GBs.

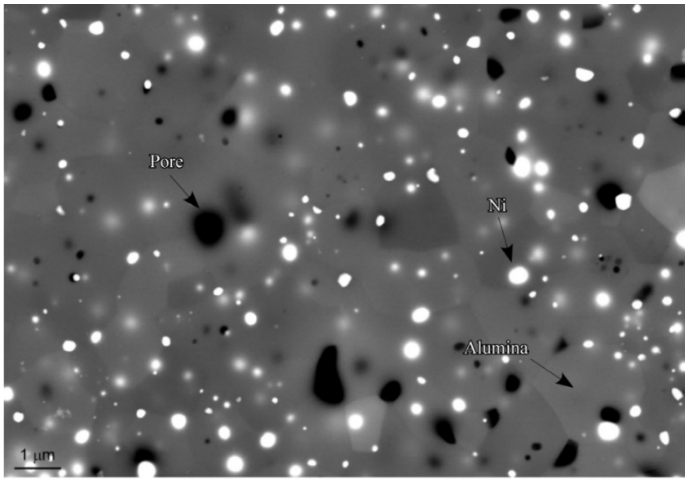

Figure 17: Backscattered HRSEM micrograph of the microstructure of Ni-alumina.

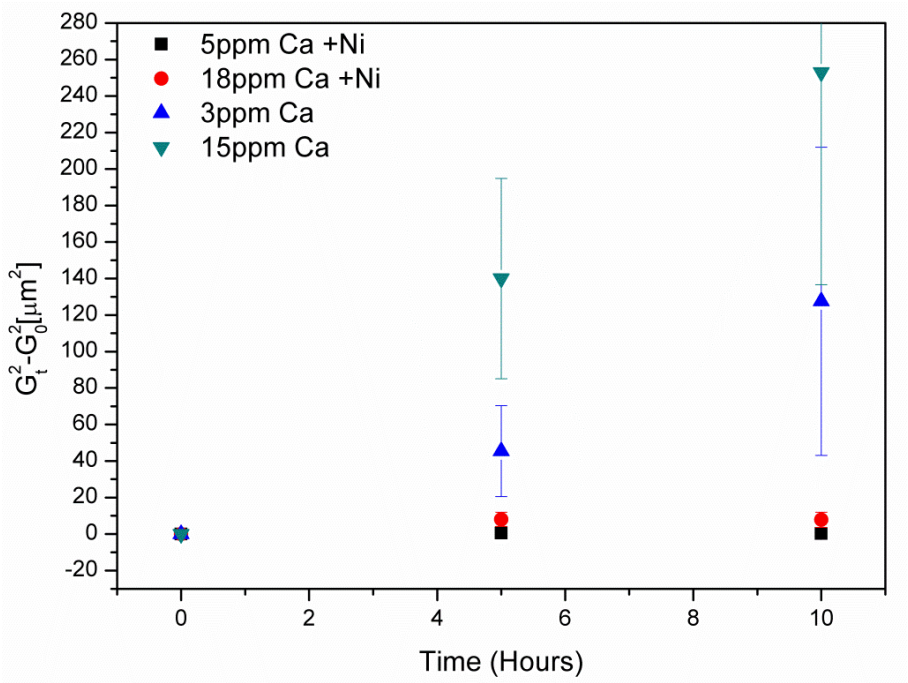

Figure 18: Grain size as function of time of undoped alumina and alumina doped with 15 ppm of Ca, compared with the grain size as function of time of undoped Ni-alumina and Ni-alumina doped with 18 ppm of Ca.

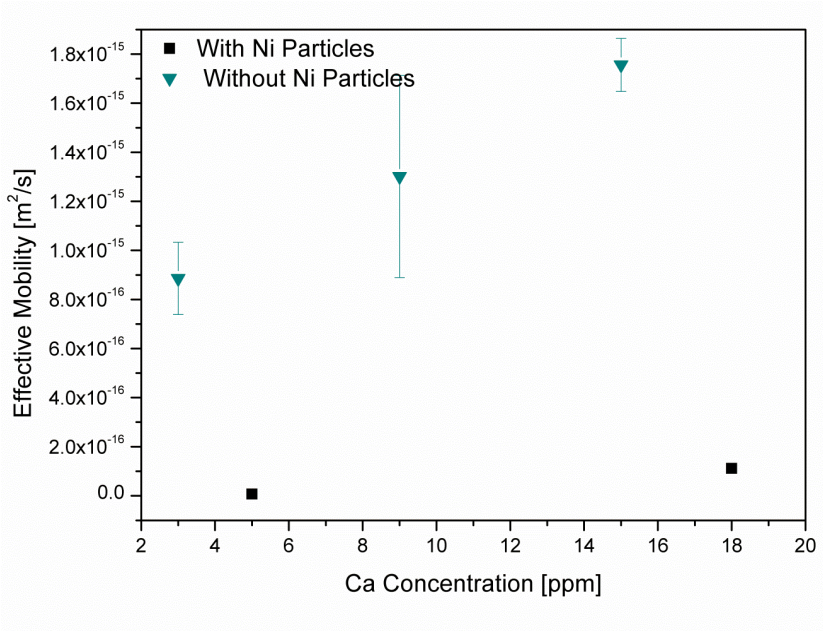

Figure 19: The effective grain boundary mobility as a function of dopant concentration (calcium) of alumina (marked ▼), and Ni-alumina (marked ■).

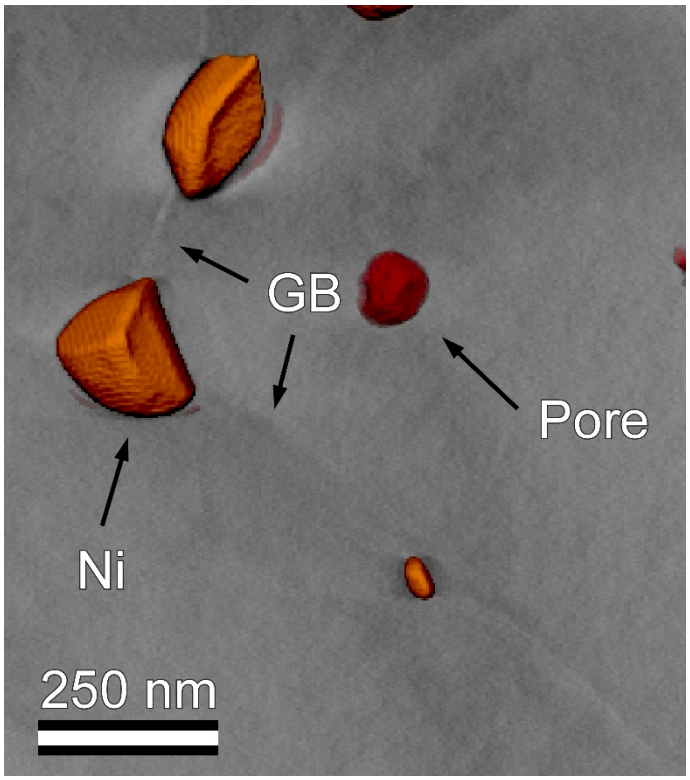

Figure 20: STEM EDS tomography micrograph of Ni particles at alumina GB. The curved facets indicate that the particles were dragged by alumina GBs.

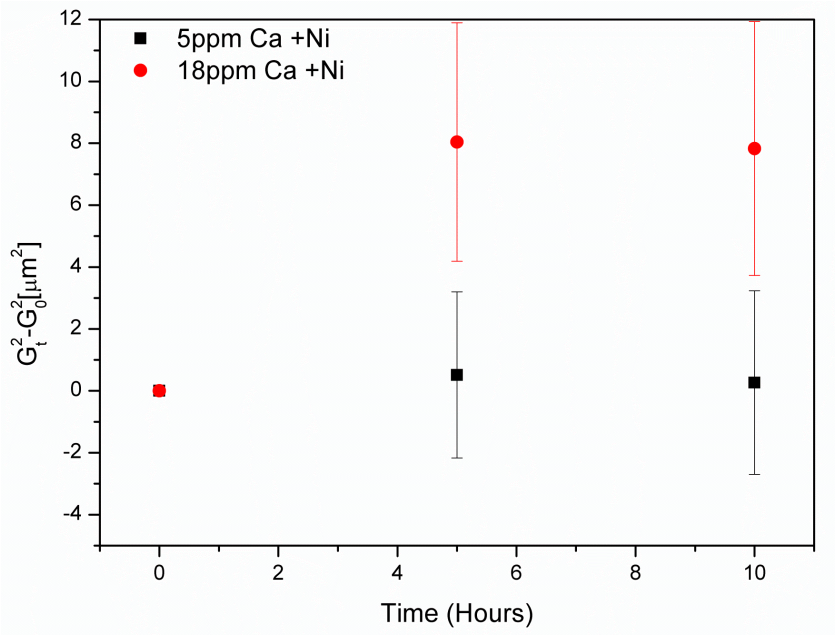

Figure 21: Grain size as function of time for undoped Ni alumina composites compared with the grain size as function of time of Ni alumina composites doped with 18 ppm of Ca.

4.4 The Influence of Dopants on Ni Occlusion in Ni-Alumina Composites

The sintered samples were found to be fully dense from the Archimedes method (according to ASTM C830). Ni-alumina samples doped with Cr_2O_3 and MgO were examined as described hereinafter to establish the influence of Cr_2O_3 on the final microstructure. Figure 22 shows a representative secondary electron (SE) HRSEM micrograph from a cross-section of a Ni-alumina sample doped with Cr_2O_3 and MgO which was annealed for 4 hours at 1250° C in He to expose the grain boundaries. The alumina grain size was determined to be 2.1±0.3 μm. Figure 24 shows a representative TEM micrograph acquired for Ni particle occlusion analysis. The location (occluded/non occluded) and size of particles was documented as summarized in Table 5. Figure 25 presents the Ni particle size distribution.

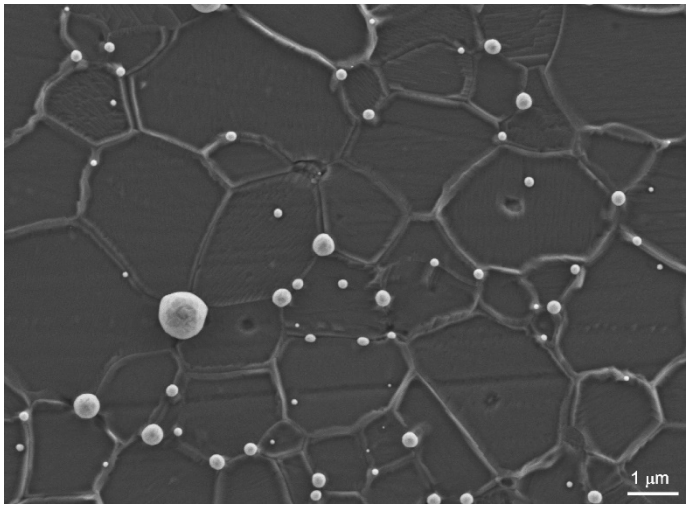

Figure 22: SE HRSEM micrograph of the microstructure of Ni-alumina doped with Cr_2O_3 and MgO.

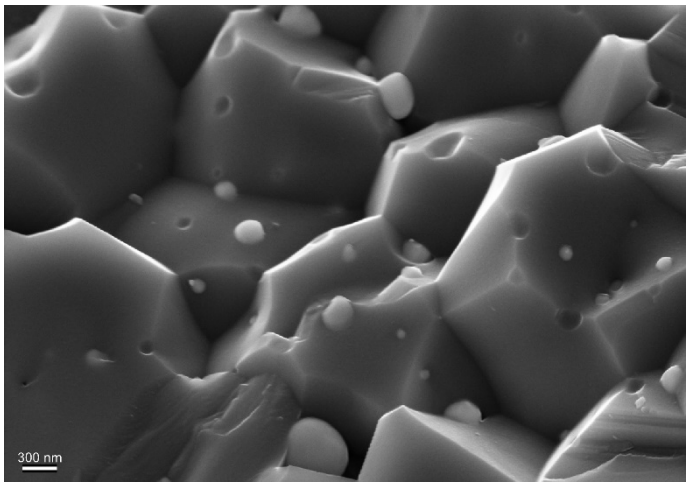

Figure 23: SE HRSEM micrograph of the fracture surface of Ni-alumina doped with Cr_2O_3 and MgO.

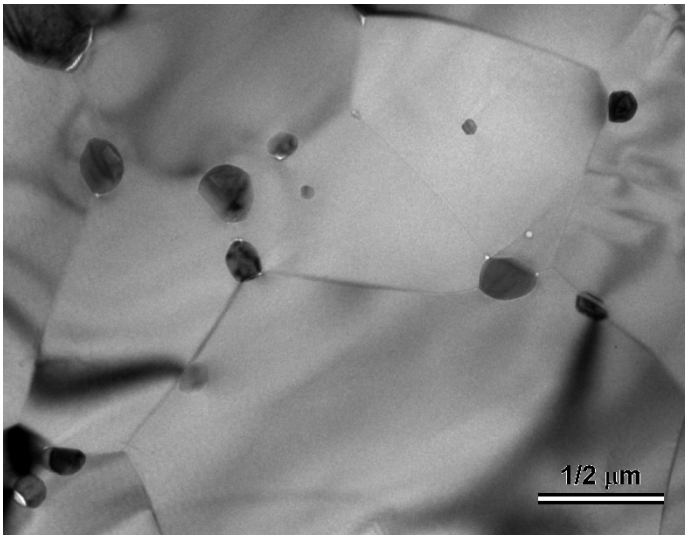

Figure 24: BF TEM micrograph of Ni-alumina doped with Cr_2O_3 and MgO.

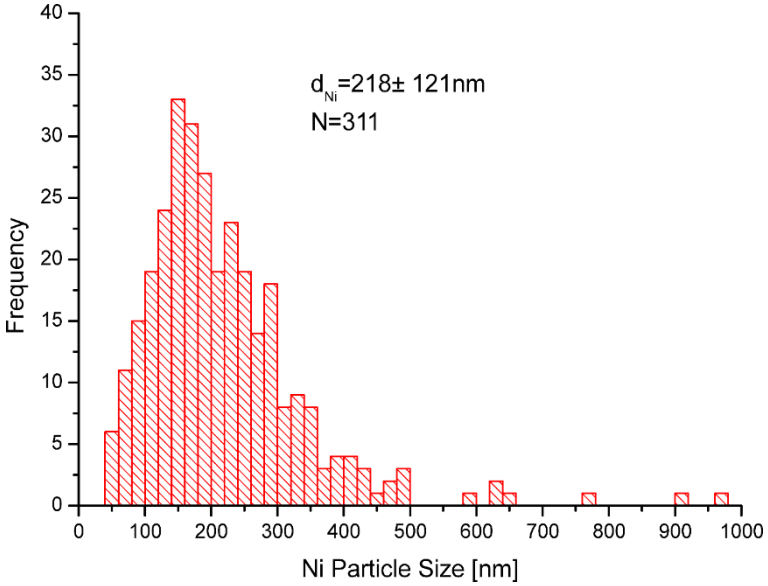

Figure 25: Ni particle size in Al_2O_3 doped with MgO and Cr_2O_3.

Table 5: Ni particle size and percent of occluded particles for Mg doped alumina, with Cr

System	Ni Particle Size [nm]	Occlusion [%]	Alumina Grain Size [μm]
Mg & Cr Doped Ni-Alumina	210±121	28	2.1±0.3

5. Discussion

5.1 The Influence of Solute on Mobility

There are various possible modes for a solute to influence grain growth in alumina, as described schematically in Figure 26 and Figure 27. The first is conventionally known as solute drag, and is most often described using Cahn's theory [3]. In this classic case, a solute in alumina will cause grain boundaries to migrate slower so as not to detach from the solute cloud, hindering their movement and leading to a reduced grain size and finer microstructure. This trend is described in blue in Figure 26 and Figure 27. From the results described in this work, an accelerating trend is also revealed. In this case, as more solute is added the mobility of the grain boundaries increases. This trend is shown in Figure 26 and Figure 27 in red. Both of these trends discontinue near the solubility limit, where an abrupt decrease in mobility is expected due to a complexion transition at the grain boundaries. As described in Figure 26, the complexion transition and decrease in mobility will occur at a specific concentration for each grain boundary. Taking into account all the complexion transitions in a polycrystalline material, one should expect to find a change in the trend as the concentration increases, and instead of an increase in mobility, a decrease in mobility is expected (Figure 27).

In addition to the influence of a solute on grain boundary mobility in alumina, this work also studied the influence of a solute on grain boundary mobility in a particle reinforced alumina matrix composite, where Zener drag is active. It is concluded that when using an accelerating solute, such as Ca, higher values of grain boundary mobilities are expected, even though the

second phase particles serve to drag the boundaries. The difference between the mobility with an accelerating solute compared to the mobility of an undoped composite will increase as the solute concentration increases. In the following sections, an explanation for the trends will be given.

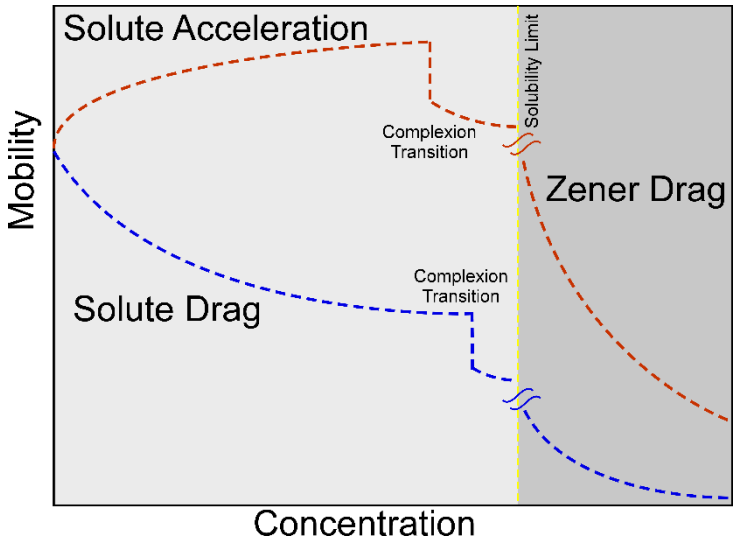

Figure 26: The influence of composition on the mobility of a single grain boundary.

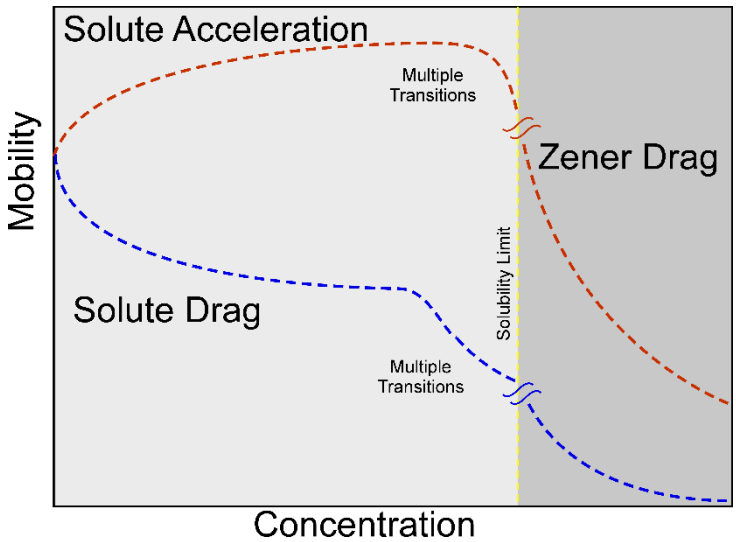

Figure 27: The influence of composition on the mobility in a polycrystalline material (with many grain boundaries).

5.2 The Influence of Solute on Alumina

5.2.1 Solute Drag

The solute drag theory was quantitatively formulated by Lücke and Detret and was further developed by Cahn and Lücke and Stüwe [12,16,64,65]. This theory has been widely accepted and has been used to explain how impurities which segregate to grain boundaries help control the microstructure of polycrystalline materials by hindering grain growth. In this way, the decrease of alumina grain boundary mobility after doping with MgO has been explained based on grain boundary segregation and solute drag (for dopant levels without second phase particles) [66, 67, 68].

Following Gibbs for a segregating dopant, as the concentration of a dopant is increased in the bulk, adsorption of the dopant at the interface/grain boundary will increase as well. At certain concentrations, first order transitions are possible, and are characterized by discontinuous changes in boundary concentrations and/or structures [6,24]. Grain boundary mobility has been predicted by Dillon et al. to be affected by these first order transitions [69].

In addition to the development of concepts that discuss the changes in grain boundary chemistry and structure (complexions), the mechanism for grain boundary movement has also been the focus of discussion in the literature [27,70]. Recently, Han et al. described how the motion of disconnections enables grain boundary movement. A disconnection is a line defect at a grain boundary (or interface) and is defined by a dislocation and/or a step character [25]. The dislocation enables grain boundary sliding and the step facilitates grain boundary

migration. The presence of solute atoms at the grain boundary may influence the motion of disconnections [24]. Disconnections do not describe the movement of atoms *along* the grain boundary (i.e. grain boundary diffusion), yet they can be used to describe the movement of atoms *across* the grain boundary, D_{GB} and D_S in equation (9). As one can deduce from equation (9), as these diffusion coefficients decrease, the grain boundary mobility will decrease as well. Also, it is conventional wisdom that the addition of solute atoms obstructs the step and dislocation movement and therefore an explanation from grain boundary kinetic behavior to solute drag is provided.

However, the solute drag model does not agree with several experimental results, including the results published in this study, which indicate that the presence of some impurities below the solubility limit *increases* the grain boundary mobility. As shown above, doping alumina with Ca increases the grain boundary mobility, and the mobility increases as a function of Ca content (Figure 16).

5.2.2 Solute Acceleration

The influence of doping alumina with MgO was studied by Coble [71]. In his study he demonstrated that the addition of MgO resulted in grains that are equiaxed, relatively small, and had a homogenous and normal grain size distribution. These observations were linked to the increase in density that was hypothesized to result from a reduction in grain boundary mobility [40, 71]. Other experimental studies have shown that in contrast to MgO, the addition of CaO and/or SiO_2 to alumina will induce grain growth, demonstrating how an addition of

solute can accelerate grain boundary movement instead of inflicting a drag force on it, assuming that the concentration of CaO and/or SiO_2 was below the solubility limit [11,35, 37].

Recently, Zamir modified the Cahn, Lücke, and Stüwe model to express the change in mobility for a system in which the impurity is known to introduce vacancies in the matrix, and thus a vacancy excess at the grain boundaries which increases the diffusivity and therefore the grain boundary mobility [72]. This model assumes an excess of adsorbed vacancies because of the increased bulk vacancy concentration. A vacancy excess may also affect the specific mechanism (disconnection motion) responsible for grain boundary motion [70]. Grimes showed that the solution mechanism for CaO in alumina introduces oxygen vacancies [73]. Ca has been experimentally confirmed to segregate to grain boundaries in alumina [11]. In their review, Han et al. consider the different disconnection types that can preside in a crystalline system. They also state that the formation of specific disconnections depend on their activation energy, where the lower the energy the more likely a specific disconnection will form [24]. Following this, it is speculated here that Ca segregation to the grain boundaries is accompanied by an excess of vacancies; these vacancies change (reduce for the case of Ca) the activation energy to form disconnections, enabling disconnection types that are otherwise energetically unfavorable, thus increasing the grain boundary mobility.

When doping alumina with MgO, the solution reaction that has the lowest expected energy is the reaction that introduces Mg interstitials into the matrix [40,73]. It is proposed, that Mg segregation to GBs will not activate disconnections, but instead change the structure of the GB. This structure change is expected to change the energy reaction barrier for the formation of

disconnections [24]. It is suggested here that this will decrease the available disconnections and limit grain boundary mobility.

It should be noted that the mobility values for the samples studied in the present study are more than two times *slower* than for samples annealed in air [11]. The samples studied in the scope of the present work were sintered and then annealed using a graphite crucible which enriched the sintering atmosphere with carbon. Since it has been shown that carbon segregates to alumina grain boundaries, the results described here demonstrate that carbon, which is assumed to form an interstitial defect similar to Mg, also induces a solute drag effect on alumina grain boundaries [74].

Relating to the suggested explanations above, a hypothesis is proposed here that by knowing the energetically preferred compensation method of a solute in a material, one can predict the influence of that solute on grain boundary mobility. The hypothesis given here, offers an explanation as to whether solute drag or solute acceleration would be expected to occur by connecting this behavior to the compensation method. Under the assumption that a solute undergoes segregation to the GB, the energetically favorable solution reaction will transpire, and point defects will form at the GB. These defects change the energy barrier for disconnection formation. Vacancies are assumed to reduce the energy barrier and to activate disconnections, as shown by Han et al., while interstitials and substitutional atoms are expected to change the disconnections at the GB and their ability to cause GB motion [24]. In the same manner as described above for CaO, MgO and C, the influence of other solutes on alumina grain boundary mobility can be assessed under this hypothesis.

In addition to CaO, SiO_2 and TiO_2 are also known to increase grain boundary mobility and increase grain growth in alumina (for dopant concentrations which are assumed to be below the solubility limit). Dillon and Harmer showed an increase in grain boundary mobility when comparing undoped alumina to SiO_2-doped alumina in a wide range of temperatures [15]. In a study by Kebbede et al. the addition of TiO_2 to alumina increased the grain size from 1.7 μm to 5.8 μm [75]. The compensation methods of the solution mechanism for both solutes in alumina is the formation of aluminum vacancies [40]. These observations agree with the hypothesis suggested above, that the compensation method of a solute can be used to further our understanding of grain boundary kinetics. It is assumed that solutes that segregate to the grain boundary and will increase the vacancy concentration at the grain boundary (following the compensation method) will enable additional disconnection systems, thus increasing the overall mobility of the boundary.

Another system of interest that involves a solute in a ceramic is SiO_2 in yttrium aluminum garnet (YAG). It has been shown that the solution of SiO_2 in YAG is accompanied by the formation of an yttrium vacancy and that SiO_2 segregates to YAG grain boundaries [72]. It has also been shown that the grain growth rate increases as the SiO_2 content is increased [76]. Thus it is suggested that in this system, SiO_2 accelerates grain boundary mobility. The segregation of SiO_2 to YAG grain boundaries and the formation of vacancies at the grain boundaries is similar to the behavior observed for CaO, SiO_2 and TiO_2 in alumina, and via the same mechanism increases grain boundary mobility.

5.3 Influence of Solute Concentration Near the Solubility Limit on Mobility

The trend displayed in this study, which shows an increase in mobility with an increase in Ca concentration, does not hold for samples doped with 47±1 ppm of calcium (Figure 16). Since this is a dopant concentration that approaches the solubility limit (which is 51±1 ppm at 1600°C [44]), one might correlate this to an inhomogeneity in dopant distribution, resulting in localized precipitation that introduced a Zener drag force. While the Zener drag force could account for the decreased mobility of some grains, extensive TEM investigations did not reveal the presence of second phase particles at the grain boundaries or triple junctions. Precipitation is expected to occur at solute levels above the solubility limit, however precipitation also requires a critical radius for nucleation. Therefore, a calculation was carried out to establish whether precipitation under these conditions is possible. The critical radius for homogenous nucleation is calculated by balancing the interfacial energy ($\gamma_{\alpha\beta}$) with the difference in Gibbs volume energy (ΔG_v):

$$\mathbf{r^{crit} = \frac{2\gamma_{\alpha\beta}}{\Delta G_v}} \qquad [18]$$

Using an estimate based on interfacial energies measured for similar systems ($\gamma_{\alpha\beta}$~1.2 J/m^2 [77, 78]), and an enthalpy of formation to calculate the Gibbs volume energy ($\Delta H^{formation}$ =111 kJ/mole of $CaO_6Al_2O_3$ (CA6) [79]), the critical radius for nucleation for this system should be ~1.8 nm. For heterogeneous nucleation of a precipitate at a grain boundary, some grain boundary area is eradicated during precipitation, and assuming a grain boundary energy of γ_{gb}~0.5 J/m^2 [47], the critical precipitate radius will be ~ 0.7 nm. The amount of calcium

available to form a CA6 precipitate at a grain boundary was estimated by deducting the amount of Ca that segregates to a fully saturated alumina grain boundary (6.1 Ca atoms/nm^2 [44]) from the amount in a metastable oversaturated grain. From the WDS measurements the highest measured Ca concentration was 100 ppm. Thus, assuming a spherical shaped CA6 precipitate, the radius of the precipitate was calculated to be ~0.36 nm. This value is less than half of the critical radius for nucleation, hence nucleation is not expected.

So an explanation as to why the grain boundary mobility decreases at a dopant concentration of 47 ppm remains to be provided. One possible explanation is that at a certain excess the vacancy model is no longer applicable, either due to a change in the solution mechanism itself, or due to a change in the excess structure at the grain boundaries.

Following Gibbs for a segregating dopant, as the concentration of a dopant is increased in the bulk, adsorption of the dopant at the interface/grain boundary will increase as well [6,9]. Due to the anisotropic properties of alumina it is expected that the amount of calcium solute that will segregate to alumina grain boundaries will vary and be different for each grain boundary. In a study of CaO doped alumina by Akiva et al. it was demonstrated that grain boundary mobility is also anisotropic, and certain planes will grow faster [11]. Observing this leads to the conclusion that the anisotropic solute segregation plays an important role in the anisotropic grain boundary growth.

As shown by Bishop et al., transitions are plausible in adsorbate layers [6]. In the same way, first order transitions that are manifested as an abrupt change in chemical excess and/or chemical structure at a surface/interface, are expected at grain boundaries [8,9]. The

anisotropic segregation of solute and the anisotropic structure of grain boundaries in alumina will therefore lead to complexion transitions to occur at different solute concentrations. In the case of a system compound with a solute accelerator, it is suggested here that the influence of transitions forming single or multi layered adsorbates will decay the movement of disconnections and may reduce grain boundary mobility. Since alumina is anisotropic, it is to be expected that for each grain boundary (or for each associated grain boundary energy), a specific concentration will trigger a complexion transition. Thus, a difference in mobility will be observed as these moving disconnections are 'deactivated' (Figure 26). When measuring the mobility of a polycrystalline material, these transitions and the influence they have on measured grain boundary mobility are averaged out and a declining slope is expected (as shown schematically in Figure 27 and in the results of this study in Figure 16).

5.4 The Influence of Solute on Alumina Composites

5.4.1 Solute Acceleration and Zener Drag

In this work, an insight as to how solute and particles influence the evolving microstructure of Ni-alumina was provided. From the results, it is clear that Ni particles result in a Zener drag force on alumina grain boundaries (Figure 19). In addition, the accelerating solute influence is also distinct, and an increase in grain growth is seen in the presence of Ca (Figure 21). The mechanism by which a solute accelerates or hinders grain boundary motion is the same. As in the non-composite samples, solute segregates to grain boundaries, and if the compensation methods dictate, a vacancy will form and a disconnection that was otherwise inactive (or not present) turns mobile (or is formed). Or, interstitials are formed, the GB structure changes, disconnections become inactive and the mobility is hindered.

In contrast to a system that includes only a solution, in a composite system additional interactions of the solute with all components of the system should be addressed. Specifically, the relationship between the solute and particles, their mobility characteristics (accelerating or dragging) and the solute-particle interface energy compared with solute-matrix grain boundary energy. Also, the relationship between different solutes is of interest. This will impact the way solute activates and/or deactivates disconnections and the resulting grain boundary mobility.

The solubility limit of Mg in an alumina sample that was co-doped with Ca and equilibrated at 1600°C is 210 ppm. This value is *higher* than the Mg solubility limit measured at the same temperature, using the same method, in a sample that does not contain Ca (132 ppm [43]). In contrast, the solubility limit of Ca in an alumina sample that was co-doped with Mg and equilibrated at 1600°C is 32 ppm, compared to 51 ppm in an alumina sample that contained only Ca [44]. Therefore, the amount of Mg in solution increases, and that of Ca is reduced, when both Ca and Mg are present in the system. This contradicts the hypothesis by Handwerker et al. suggesting that adding Mg to alumina increases the solubility limit of cations that form liquid phases [35].

The role of Mg in alumina is accepted in the literature to be segregation to grain boundaries, where solute-drag reduces grain boundary mobility [95]. Considering the measured solubility limits mentioned above, it can be inferred that when doping alumina with MgO, interstitials are introduced in the grain boundary region in addition to within the bulk alumina. It is assumed here that interstitials in the grain boundary region result in a solute-drag force that reduces grain boundary mobility. When MgO-doped alumina is co-doped with CaO, the

vacancy concentration in the bulk increases, increasing the bulk diffusivity [7340]. It is assumed here that the vacancy excess at the grain boundaries increases with an increased bulk vacancy activity, which should increase the grain boundary diffusivity and grain boundary mobility by changing the disconnections [9,72].

The samples which contained both MgO and CaO showed a significant increase in the Mg solubility limit and a decrease in the Ca solubility limit. The increase in the Mg solubility limit indicates that the concentration of Mg in the bulk can reach higher values in the presence of CaO. Therefore, following Gibbsian adsorption, more Mg atoms are available to segregate to the grain boundaries and the drag force on grain boundaries is increased. This provides an explanation for the experimentally known fact that doping alumina with MgO limits grain growth (in addition to promoting sintering) even in the presence of Ca. Since Ca is often present as an impurity in alumina, even at the highest purity grade, its presence increases the solute drag force that Mg exacts on alumina grain boundaries by increasing Mg solubility and Mg segregation to grain boundaries.

Table 6 summarizes the various possibilities for the influence of Mg and/or Ca on the grain boundary mobility of alumina. The underlining assumption for all suggested possibilities is that an increase in Mg and/or Ca bulk concentration leads to an increase in Mg and/or Ca grain boundary excess. While there is a clear influence of one dopant on the solubility limit of the second, it is not known how one dopant affects the adsorption profile of the second, and at this point this issue is ignored. Table 6 demonstrates how Mg at dopant concentrations below the solubility limit can be used to limit grain growth, where Ca at concentrations below the solubility limit causes an increase in grain growth rates. However, Mg reduces the negative

influence of Ca, since co-doping leads to a higher amount of Mg in solution and thus a higher amount contributing to solute-drag at grain boundaries. This is schematically described in Figure 28.

Table 6: The influence of Mg and Ca on grain growth of alumina as single species and in co-doping conditions.

System	Mg Concentration [above/below solubility limit]	Ca Concentration [above/below solubility limit]	Mechanism	Grain Boundary Behavior
Mg doped alumina	Above	-	Zener drag resulting from precipitation of $MgAl_2O_4$	Decreased grain boundary mobility
Mg doped alumina	Below	-	Solute-drag: Segregation of Mg interstitials to grain boundaries	Decreased grain boundary mobility
Ca doped alumina	-	Above	Zener drag resulting from precipitation of $CaO{\cdot}6Al_2O_3$	Decreased grain boundary mobility
Ca doped alumina	-	Below	Solute-acceleration resulting from segregation of Ca to grain boundaries, presumably increasing the grain boundary vacancy concentration	Increased grain boundary mobility
Co-doped alumina (Mg & Ca)	Above	Above	Zener drag resulting from secondary phases	Decreased grain boundary mobility
	Below	Above	Zener drag resulting from secondary phases	Decreased grain boundary mobility
	Above	Below	Zener drag resulting from secondary phases and solute acceleration due to Ca segregation.	Unknown
	Below	Below	Solute-drag due to segregation of Mg dominates over solute-acceleration due to Ca segregation.	Decreased grain boundary mobility

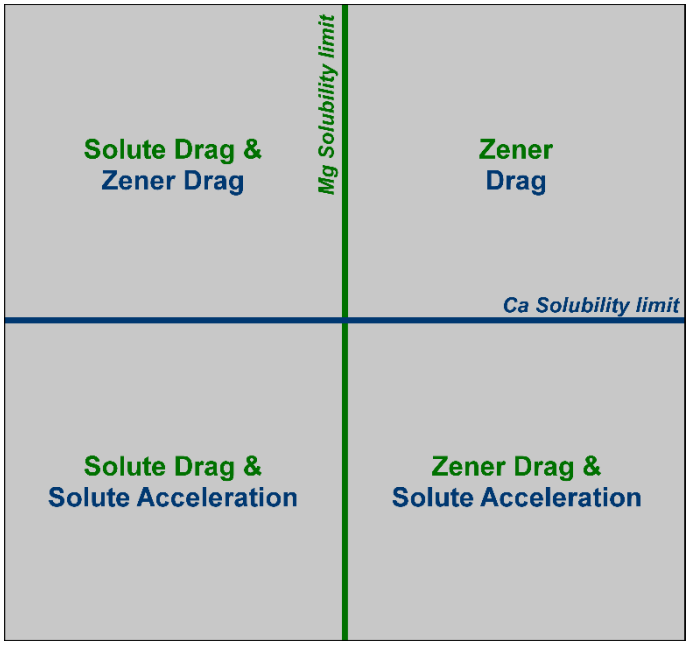

Figure 28: A schematic representation of the influence of Mg and/or Ca on grain growth of alumina as single species and in co-doping conditions.

5.4.2 The Influence of a Solute on Occlusion

Solute segregation is acute to the evolving microstructure, therefore it is reasonable to assume that this would also influence the relationship between particles and matrix grain boundaries. This was demonstrated by Gluzer et al. as they showed the segregation of Mg to Ni-alumina interface and its effect on Ni particles. Specifically, the amount of occluded Ni particles increased compared to samples that were not doped with MgO. Since MgO is known as a dragging solute, it was hypothesized that the segregation of Mg to the Ni-alumina interface reduced the amount of Mg available for segregation to grain boundaries. Thus, the drag force is reduced, grain boundaries move faster than particles, and after detachment they are occluded [47].

To broaden the understanding of how a solute influences the microstructure, Ni-alumina samples were doped with MgO and Cr_2O_3. Pursuant to this it was discovered that alumina grain size of ($MgO \cdot Cr_2O_3$) doped Ni-alumina is approximately the same grain size measured in MgO doped Ni-alumina samples, and the amount of Ni particles that were occluded was similar in both systems [47]. This contradicts evidence that the addition of Cr to alumina inhibits alumina grain growth [80]. It is offered here that the fully soluble Cr_2O_3 in MgO doped Al_2O_3 does not change the disconnections in alumina, neither at the grain boundaries nor at Ni-alumina interface. MgO segregates to alumina grain boundaries and/or Ni-alumina interfaces to reduce energy. Cr, however, replaces Al in Al_2O_3 and Cr_2O_3 is fully soluble in Al_2O_3. Therefore, it is proposed that Cr segregation will not reduce the GB energy more than Mg will, and Cr segregation will not be energetically favorable. Consequently, a difference in mobility and occlusion occurrences is not expected.

6. Summary and Conclusions

The goal of this research was to study the influence dopant and particles have on the evolving microstructure of alumina. This was accomplished by examining the influence solutes have on the GB mobility of alumina and alumina incorporated with Ni particles. Solutes were chosen to revisit the solute drag theory and it was demonstrated that the influence of solutes is not as straight forward as the solute drag predicts.

The mobility of alumina grain boundaries was measured in samples that were doped with an increasing amount of Ca, below the solubility limit. A trend of increasing mobility with increasing dopant content was measured, contradicting the conventional solute drag theory. The increase in mobility in Ca doped samples was also shown in a composite system where particles inflict a Zener drag force on grain boundaries. These results indicate that the solute drag theory may not apply to all systems, and that a further understanding of the role of dopants in microstructural evolution is required. An alternative explanation for the influence of cations on grain boundary mobility was provided. It was shown that Ca segregation to alumina GBs occurs and that the compensation method most likely to transpire is that of vacancy formation. By recognizing that GB movement occurs by the movement of disconnections, it was speculated that the presence of vacancies enables the activation of disconnections that were otherwise stagnate. Thus, explaining the increased GB mobility in a system that is doped with solute that forms vacancies. The trend presented in this study enables the prediction of grain growth behavior in Ca-doped alumina at a range of concentrations below the solubility limit,

specifically. Extensively, the prediction of the influence of solutes on GB is also enabled by knowledge of the solute compensation method.

In order to broaden the scope of this research, Mg was chosen to investigate solutes that are known to inhibit grain boundary mobility, and the combined influence of Ca and Mg in alumina was studied. The solubility limit of Ca and Mg co-doped in alumina at 1600°C was studied and determined to be 32 ppm of Ca and 210 ppm of Mg. The solubility limits of the cations in co-doped alumina were different than those in singly doped alumina. Specifically, the solubility limit of Ca is lower in the presence of Mg, and the solubility limit of Mg in alumina is higher in the presence of Ca. These results indicate that in co-doped alumina the Mg concentration in the grains will increase, and the amount of Mg excess to exert a solute drag-force on alumina grain boundaries should also increase, resulting in a decrease in grain boundary mobility. The compensation method of Mg in alumina was examined, and it was found that Mg introduces interstitials in alumina. The drag force that Mg inflicts on alumina grain is thus explained by introducing interstitials at the grain boundary, which change and obstruct the movement of disconnections and deactivates them. This is proposed as the mechanism by which Mg decreases grain growth in alumina containing Ca impurities, as opposed to previous hypotheses that speculated that the presence of MgO prevents glass aluminate phase formation.

7. Recommendations for Future Work

Further work on the influence calcium has on alumina grain boundary mobility and the transitions that occur with increasing dopant concentration should be completed. Due to the anisotropic nature of alumina, an adequate study would entail an investigation of the mobility of a specific grain boundary plane at an increasing bulk concentration of calcium that will lead to an increase in adsorption at the alumina grain boundary.

Additional research is needed to establish the influence of Mg on alumina grain boundary mobility at concentrations below the solubility limit. Also, the amount of *segregating* Mg to alumina grain boundaries needed to change the grain boundary mobility should be investigated. Different grain boundary planes have been shown to behave differently and some are more prone to Ca segregation than others which can also influence their mobility [11]. Therefore, a correlation between grain boundary plane and segregating cation concentration is needed to understand the influence Mg and/or Ca have on the onset of abnormal grain growth.

To broaden the understanding of the influence of dopants on particle occlusion, the particle-matrix interface should be studied. Specifically, comparing the amount of Mg segregation to Ni-alumina interface to the amount of Mg segregation to alumina GB may give insight regarding the higher occlusion rate that was reported when doping Ni-alumina with MgO.

Finally, while in this work the defect chemistry evaluated by Grimes et al. [73] is used to explain possible mechanisms for accelerated or decelerated grain boundary mobility, the motion of disconnections in the plane of grain boundaries has been hypothesized to be the mechanism of grain growth [23-26]. The atomistic mechanism by which dopant cations such as Mg and Ca influence the formation and/or motion of disconnections may be critical to fully understand solute-drag and solute-acceleration phenomena.

8. References

1. P. S. de Laplace, H. H. Harte. A Treatise of Celestial Mechanics. R. Milliken, Dublin, 1822.

2. J. E. Taylor, II—Mean Curvature and Weighted Mean Curvature, Acta Metallurgica et Materialia 40, 1475-1485 (1992).

3. J. D. Powers, A. M. Glaeser, Grain Boundary Migration in Ceramics, Interface Science, **6**[1-2]:23-39, 1998.

4. J. E. Burke, D. Turnbull, Recrystallization and Grain Growth, Progress in Metal Physics, **3**[0]:220-292, 1952.

5. M. N. Rahaman. Ceramic Processing and Sintering. Taylor & Francis, 2003. p.557-615.

6. C. M. Bishop, M. Tang, R. M. Cannon, W. C. Carter, Continuum Modelling and Representations of Interfaces and Their Transitions in Materials, Materials Science and Engineering: A, **422**[1–2]:102-114, 2006.

7. M. P. Seah, E. D. Hondros, Use of a "BET" Analogue Equation to Describe Grain Boundary Segregation, Scripta Metallurgica 7, 735-737 (1973).

8. S. J. Dillon, M. Tang, W. C. Carter, M. P. Harmer, Complexion: A New Concept for Kinetic Engineering in Materials Science, Acta Materialia 55, 6208-6218 (2007).

9. W. Kaplan, D. Chatain, P. Wynblatt, W. C. Carter, A Review of Wetting Versus Adsorption, Complexions, and Related Phenomena: The Rosetta Stone of Wetting, Journal of Materials Science, **48**[17]:5681-5717, 2013.

10. M. F. Yan, R. M. Cannon, H. K. Bowen. Grain Boundary Migration in Ceramics, In: Ceramic Microstructure ′76, Fulrath RM, Pask JA, Boulder, editors CO: Westview Press, 1977. p.276–307.

11. R. Akiva, A. Katsman, W. D. Kaplan, Anisotropic Grain Boundary Mobility in Undoped and Doped Alumina, Journal of the American Ceramic Society, **97**[5]:1610-1618, 2014.

12. K. Lücke, H. P. Stüwe, On the Theory of Impurity Controlled Grain Boundary Motion, Acta Metallurgica, **19**[10]:1087-1099, 1971.

13. J. W. Cahn. The Impurity-Drag Effect in Grain Boundary Motion. The Selected Works of John W. Cahn. John Wiley & Sons, Inc., 2013. p.115-116.

14. M. Hillert, B. Sundman, A Treatment of the Solute Drag on Moving Grain Boundaries and Phase Interfaces in Binary Alloys, Acta Metallurgica, **24**[8]:731-743, 1976.

15. S. J. Dillon, M. P. Harmer, Relating Grain Boundary Complexion to Grain Boundary Kinetics II: Silica-Doped Alumina, Journal of the American Ceramic Society, **91**[7]:2314-2320, 2008.

16. A. M. Glaeser, H. K. Bowen, R. M. Cannon, Grain-Boundary Migration in LiF: I, Mobility Measurements, Journal of the American Ceramic Society, **69**[2]:119-126, 1986.

17. C. Zener, C. S. Smith, Grains, Phases, and Interfaces- an Interpretation of Microstructure, Transactions of the Metallurgical Society of Aime, **175**[15], 1948.

18. D. Turnbull, Theory of Grain Boundary Migration Rates. Transactions of AIME 191, 661-665 (1951).

19. N. F. Mott, Slip at Grain Noundaries and Grain Growth in Metals, Proceedings of the Physical Society **60**, 391-394 (1948).

20. S. E. Babcock, R. W. Balluffi, Grain Boundary Kinetics—I. In Situ Observations of Coupled Grain Boundary Dislocation Motion, Crystal Translation and Boundary Displacement, Acta Metallurgica **37**, 2357-2365 (1989).

21. J. W. Cahn, Theory of Crystal Growth and Interface Motion in Crystalline Materials, Acta Metallurgica **8**, 554-562 (1960).

22. S. J. Zheng, X. L. Ma, T. Yamamoto, Y. Ikuhara, Atomistic Study of Abnormal Grain Growth Structure in BaTiO3 by Transmission Electron Microscopy and Scanning Transmission Electron Microscopy, Acta Materialia **61**, 2298-2307 (2013).

23. Gleiter H. The Mechanism of Grain Boundary Migration, Acta Metall. 1969; 17 (5): 565-573.

24. J. Han, S. L. Thomas, D. J. Srolovitz, Grain-Boundary Kinetics: A Unified Approach, Progress in Materials Science, **98**, 386-476, 2018.

25. Hirth JP, Pond RC. Steps, Dislocations and Disconnections as Interface Defects Relating to Structure and Phase Transformations, Acta Mater. 1996;44(12):4749-63.

26. Khater HA, Serra A, Pond RC, Hirth JP. The Disconnection Mechanism of Coupled Migration and Shear at Grain Boundaries, Acta Mater. 2012;60(5):2007-20.

27. H. Gleiter, Theory of Grain Boundary Migration Rate, Acta Metallurgica 17, 853-862 (1969).

28. I. Levin, D. Brandon, Metastable Alumina Polymorphs: Crystal Structures and Transition Sequences, Journal of the American Ceramic Society, 81[8]:1995-2012, 1998.

29. W. H. Gitzen. Alumina as a Ceramic Material. Wiley, 1970.

30. M. L. Kronberg, Plastic Deformation of Single Crystals of Sapphire: Basal Slip and Twinning, Acta Metallurgica, 5[9]:507-524, 1957.

31. E. Dörre, H. Hübner. Alumina: Processing, Properties, and Applications. Springer-Verlag, 1984. p.5,193

32. H. E. Swanson, E. Tatge, R. K. Fuyat. Standard X-ray Diffraction Powder Patterns, 1953.

33. M. Lieberthal, W. D. Kaplan, Processing and Properties of Al_2O_3 Nanocomposites Reinforced with Sub-micron Ni and $NiAl_2O_4$, Materials Science and Engineering A, **302**[1]:83-91, 2001.

34. P. Boch, T. Chartier. Alumina, Mullite and Spinel, Zirconia, Ceramic Materials. ISTE, 2010. p.199-230.

35. Handwerker CA, Morris PA, Coble RL. Effects of Chemical Inhomogeneities on Grain Growth and Microstructure in Al_2O_3, J. Am. Ceram. Soc. 1989; 72(1):130-136.

36. Altay A, Gülgün MA. Microstructural Evolution of Calcium-doped α-alumina, J. Am. Ceram. Soc. 2003; 86(4):623-29.

37. Bae SI, Baik S. Determination of Critical Concentrations of Silica and/or Calcia for Abnormal Grain Growth in Alumina, J. Am. Ceram. Soc. 1993; 76(4):1065-1067.

38. Berry KA, Harmer MP. Effect of MgO Solute on Microstructure Development in Al_2O_3, J. Am. Ceram. Soc. 1986; 69(2):143-149.

39. Bennison SJ, Harmer MP. Effect of MgO Solute on the Kinetics of Grain Growth in Al_2O_3, J. Am. Ceram. Soc. 1983; 66(5):C90-C92.

40. Johnson WC, Coble RL. A Test of the Second-phase and Impurity-Segregation Models for MgO-enhanced Densification of Sintered Alumina, J. Am. Ceram. Soc. 1978; 61 (3-4):110-114.

41. Ji Y, Yeomans JA. Microstructure and Mechanical Properties of Chromium and Chromium/Nickel Particulate Reinforced Alumina Ceramics, J. Mater. Sci. 2002; 37(24):5229-5236.

42. Kingery WD. Densification During Sintering in the Presence of a Liquid Phase. I. Theory, J. Appl. Phys. 1959; 30(3):301-306.

43. Miller L, Avishai A, Kaplan WD. Solubility Limit of MgO in Al_2O_3 at 1600°C, J. Am. Ceram. Soc. 2006; 89(1):350-353.

44. Akiva R, Berner A, Kaplan WD. The Solubility Limit of CaO in α-alumina at 1600°C, J. Am. Ceram. Soc. 2013; 96(10):3258-3264.

45. Dillon SJ, Behera SK, Harmer MP. An Experimentally Quantifiable Solute Drag Factor, Acta Mater. 2008; 56(6):1374-1379.

46. S. J. L. Kang. Sintering: Densification, Grain Growth and Microstructure. Elsevier Science, 2004.

47. G. Gluzer, W. D. Kaplan, Particle Occlusion and Mechanical Properties of Ni–Al_2O_3 Nanocomposites, Journal of the European Ceramic Society 33 (15–16) (2013) 3101-3113.

48. S. J. Dillon, M. P. Harmer, Relating Grain-Boundary Complexion to Grain-Boundary Kinetics I: Calcia-Doped Alumina, Journal of the American Ceramic Society, **91**[7]:2304-2313, 2008.

49. A. Avishai, W. D. Kaplan, Intergranular Films in Metal-Ceramic Composites and the Promotion of Metal Particle Occlusion, Z. Metallk. **95**, 266-270 (2004).

50. I. J. Bae, S. Baik, Abnormal Grain Growth of Alumina, Journal of the American Ceramic Society, **80**[5]:1149-1156, 1997.

51. S.-H. Lee, D.-Y. Kim, N. M. Hwang, Effect of Anorthite Liquid on the Abnormal Grain Growth of Alumina, Journal of the European Ceramic Society, **22**[3]:317-321, 2002.

52. C. W. Park, D. Y. Yoon, Effects of SiO2, CaO2, and MgO Additions on the Grain Growth of Alumina, Journal of the American Ceramic Society, **83**[10]:2605-2609, 2000.

53. A. Avishai, W. D. Kaplan, Intergranular Films at Metal–Ceramic Interfaces: Part II – Calculation of Hamaker Coefficients, Acta Materialia, 53[5]:1571-1581, 2005.

54. G. Gottstein, L. S. Shvindlerman, On the Retardation of Grain Boundary Motion by Small Particles, Scripta Materialia, **63**[11]:1089-1091, 2010.

55. M. I. Mendelson, Average Grain Size in Polycrystalline Ceramics, Journal of the American Ceramic Society, **52**[8]:443-446, 1969.

56. Lieberthal, M. and W.D. Kaplan, Processing and Properties of Al_2O_3 Nanocomposites Reinforced with Sub-micron Ni and $NiAl_2O_4$, Materials Science and Engineering: A, 2001. 302(1): p. 83-91.

57. O. Aharon, S. Bar-Ziv, D. Gorni, T. Cohen-Hyams, W. D. Kaplan, Residual Stresses and Magnetic Properties of Alumina-nickel Nanocomposites, Scripta Materialia **50**, 1209-1213 (2004).

58. Goldstein J, Newbury DE, Echlin P, Joy DC, Romig Jr AD. Lyman CE, et al. Scanning Electron Microscopy and X-ray Microanalysis: A Text for Biologists, materials scientists. and geologists. Springer Science & Business Media, 2012.

59. Berner AI, Gimelfarb FA, Ukhorskaya TA. Metrological Aspects of Micro-probe Analysis, J. Anal. Chem. 1982; 37(2):268-276.

60. Merlet C., An Accurate Computer Correction Program for Quantitative Electron Probe Microanalysis, Microchim. Acta. 1994; 114-115(1):363-376.

61. V. J. Keast, D. B. Williams, Quantification of Boundary Segregation in the Analytical Electron Microscope, Journal of Microscopy **199**, 45-55 (2000).

62. C. Scheu, W. Stein, M. Rühle, Electron Energy-Loss Near-Edge Structure Studies of a Cu/(11-20)α-Al2O3 Interface, physica status solidi (b) **222**, 199-211 (2000).

63. C. Scheu, Electron Energy-loss Near-edge Structure Studies at the Atomic Level: Reliability of the Spatial Difference Technique, Journal of Microscopy, **207**, 52-57 (2002).

64. J. W. Cahn, The Impurity-drag Effect in Grain Boundary Motion, Acta Metallurgica 10 (9) (1962) 789-798.

65. K. Lücke, K. Detert, A Quantitative Theory of Grain-Boundary Motion and Recrystallization in Metals in the Presence of Impurities, Acta Metallurgica **5**, 628-637 (1957).

66. H. L. Marcus and M. E. Fine, Grain-Boundary Segregation in MgO-doped Al_2O_3, Journal of the American Ceramic Society 55 (11) (1972) 568-570.

67. K. L. Gavrilov, S. J. Bennison, K. R. Mikeska, J. M. Chabala and R. Levi-Setti, Silica and Magnesia Dopant Distributions in Alumina by High-Resolution Scanning Secondary Ion Mass Spectrometry, Journal of the American Ceramic Society 82 (4) (1999) 1001-1008.

68. K. L. Gavrilov, S. J. Bennison, K. R. Mikeska and R. Levi-Setti, Grain Boundary Chemistry of Alumina by High-Resolution Imaging SIMS, Acta Materialia 47 (15-16) (1999) 4031-4039.

69. S. J. Dillon, M. P. Harmer, Relating Grain-Boundary Complexion to Grain-Boundary Kinetics I: Calcia-doped Alumina. Journal of the American Ceramic Society 91, 2304-2313 (2008).

70. H. Sternlicht, W. Rheinheimer, M. J. Hoffmann, W. D. Kaplan, The Mechanism of Grain Boundary Motion in SrTiO3, Journal of Materials Science 51, 467-475 (2016).

71. R. L. Coble. Transparent Alumina and Method of Preparation. US Patent Office US3026210A, 1962.

72. S. Zamir, Si Segregation and its Role in Reaching Transparent YAG, Journal of the American Ceramic Society 100 (4) (2017) 1689-1696.

73. R. W. Grimes, Solution of MgO, CaO, and TiO_2 in α-Al_2O_3, Journal of the American Ceramic Society 77 (2) (1994) 378-384.

74. E. A. Marquis, N. A. Yahya, D. J. Larson, M. K. Miller, R. I. Todd, Probing the Improbable: Imaging C Atoms in Alumina, Materials Today 13 (10) (2010) 34-36.

75. A. Kebbede, J. Parai, A. H. Carim, Anisotropic Grain Growth in α-Al_2O_3 with SiO_2 and TiO_2 Additions, Journal of the American Ceramic Society 83, 2845-2851 (2000).

76. A. J. Stevenson et al., Effect of SiO_2 on Densification and Microstructure Development in Nd:YAG Transparent Ceramics, Journal of the American Ceramic Society **94**, 1380-1387 (2011).

77. G. Levi and W. D. Kaplan, Aluminium-alumina Interface Morphology and Thermodynamics from Dewetting Experiments, Acta Materialia 51 (10) (2003) 2793-2802.

78. H. Meltzman, D. Chatain, D. Avizemer, T. M. Besmann, W. D. Kaplan, The Equilibrium Crystal Shape of Nickel, Acta Materialia 59 (9) (2011) 3473-3483.

79. A. Douy, M. Gervais, Crystallization of Amorphous Precursors in the Calcia–alumina System: A Differential Scanning Calorimetry Study, Journal of the American Ceramic Society 83 (1) (2000) 70-76.

80. E. Manor, Grain Growth Inhibition in Nanocrystalline Alumina Doped with Chromia, Nanostructured Materials 8, 359-366 (1997).

השפעת מסממים וחלקיקים על קינטיקת

התפתחות המיקרומבנה של אלומינה

רות משה

השפעת מסממים וחלקיקים על קינטיקת התפתחות המיקרומבנה של אלומינה

חיבור על מחקר

לשם מילוי חלקי של הדרישות לקבלת התואר דוקטור בפילוסופיה

רות משה

הוגש לסנט הטכניון – מכון טכנולוגי לישראל

חשוון התש"פ חיפה נובמבר 2019

תודות

מחקר זה נערך בהנחיית **פרופ' וויין ד. קפלן** מהפקולטה למדע והנדסה של חומרים בטכניון – מכון טכנולוגי לישראל.

אני מודה לטכניון על חלקו בתמיכה הכספית בהשתלמותי. מחקר זה נתמך בחלקו על ידי הקרן הלאומית למדע (מענק מספר 1779/18). כמו כן, ברצוני להוקיר תודה למלגות ע"ש גייקובס ולמלגה ע"ש שיין על תמיכתם הכספית לאורך ההשתלמות.

תקציר

כחלק מתהליך הסינטור בחומרים קרמיים מתרחש גידול גרעינים אשר הינו חלק משמעותי מהתפתחות המיקרומבנה. מחקרים רבים עסקו בהבנת הגורמים המשפיעים על קצב גידול הגרעינים ותנועת גבולות הגרעין. התיאוריה המקובלת כיום העוסקת בהשפעתם של מסממים אשר עוברים סגרגציה במצב שיווי משקל לגבול הגרעין, על המוביליות של גבול הגרעין מניחה שנוכחות מסממים בחומר תוביל להפעלת כוח שיעכב את התקדמות הגבול והאטתו. אולם, ישנם מספר מערכות שבהן הוכח כי הנחה זו אינה מתיישבת ובמקום להאט את גבול הגרעין, נוכחות מסממים מאיצה את התקדמותו. במחקר זה נבחנה תיאוריה זו וכן הנחות היסוד בבסיס תיאוריה זו, באמצעות בחינת ההשפעה של סידן בריכוזי סימום שונים, בערכי סימום מתחת לגבול המסיסות, על התפתחות המיקרו-מבנה של אלומינה ואלומינה מרוכבת עם חלקיקי ניקל. מדידת ריכוז סימום הסידן בדגמים בוצעה על ידי ספקטרוסקופיית פיזור גל (Wavelength dispersive spectroscopy) על ידי מדידות שכוילו באמצעות דגם ייחוס. שיטת אפיון זו רגישה לריכוזים נמוכים ומאפשרת קבלת ערכי גבול גילוי נמוכים בהתאם לנדרש במדידות סידן מתחת לגבול המסיסות. כמו כן, בוצע אפיון לקביעת גודל גרעין בעזרת מיקרוסקופ אלקטרונים סורק ונמדדו ערכי המוביליות של הגרעינים כתלות בריכוז הסימום שנמדד. בניגוד למסממים שעוברים סגרגציה המאטים את ניידות גבולות הגרעין, סידן מאיץ אותם. נמצא, כי קיימת מגמה בין ריכוז הסידן להאצת גבולות הגרעין וכי ככל שריכוז הסידן עולה, עולה מוביליות הגבול גרעין. במחקר זה הועלתה השערה כי העלייה בניידות עם עליית ריכוז הסימום בסידן מקורה במנגנון יצירת העדרויות בגבול אשר מאפשר לגבולות הגרעין לנוע יותר מהר. נמצא גם כי באלומינה מרוכבת עם חלקיקי ניקל בנוסף להאטה בניידות של גבולות הגרעינים הנובעת מנוכחות חלקיקי הניקל, ניכר כי נוכחות סידן כממס, גורמת לגידול גרעינים.

בנוסף, על מנת להרחיב את ההבנה של השפעת מסממים על המיקרומבנה של אלומינה, גבול המסיסות של סיליקון (צורן) באלומינה וכן גבולות המסיסות של מגנזיום וסידן באלומינה נמדדו באמצעות ספקטרוסקופיית פיזור גל. לשם קביעת גבול המסיסות של סיליקון באלומינה ב 1600°C, הוכנו אבקות בהרכב של אלומינה וסיליקון אשר, לאחר

סינטור, יוביל לכך שבדגמים יימצאו שתי פאזות יציבות: מולייט ($mullite, 3Al_2O_3 \cdot 2SiO_2$) ואלומינה מועשרת בסיליקון. כך, ניתן להבטיח כי בעת מדידת ריכוז הסיליקון בגרעיני האלומינה למעשה נמדד ריכוז גבול המסיסות. מדידות גבול המסיסות בוצעו בדגמים שעברו חיסום וכן בדגמים שעברו תהליך של קירור איטי. עבור הדגמים שעברו חיסום נקבע כי גבול המסיסות של סיליקון באלומינה ב 1600°C הוא 188±7 ppm.

באופן דומה, גבולות המסיסות של מגנזיום וסידן, בעת סימום שניהם יחד באלומינה, בטמפרטורה של 1600°C נקבעו. במערכת זאת התייצבו הפאזות ($MgAl_2O_4$ (Mg spinel), $CaO \cdot 6Al_2O_3$ (CA6), $Ca_2Mg_2Al_{28}O_{46}$ (CAM-II) וכן אלומינה מועשרת במגזניום וסידן. מהרכב זה ניתן להסיק כי גרעיני האלומינה רווים וכי ריכוז הסידן והמגנזיום הנמדד בהם מהווה את גבולות המסיסות של קטיונים אלו באלומינה. גבול המסיסות שנמדד מדגמים אלו עבור סידן הינו 32±13 ppm וגבול המסיסות שנמדד מדגמים אלו עבור מגנזיום הינו 210±43 ppm. הנוכחות של סידן באלומינה מעלה את גבול המסיסות של מגנזיום באלומינה מ 132 ppm ל 210 ppm. מתוך כך, ניתן להסיק כי העלייה בריכוז המגנזיום כממס בגרעינים תגרום לעליית ריכוז המגנזיום שיעבור סגרגציה לגבולות גרעין ובכך יתרום לירידה בניידות.

כמו כן, נבחנה השפעת נוכחות מסממים על המיקרומבנה המתקבל בחומר מרוכב של אלומינה עם חלקיקי ניקל. בוצעה אנליזה בעזרת מיקרוסקופ אלקטרונים חודר לקביעת מיקום חלקיקי הניקל, בתוך הגרעין או בגבולות הגרעין, כתוצאה מנוכחות ממס בגרעיני האלומינה.